Spatio-temporal control of nuclear mechanotransduction during EMT

Ronan BOUZIGNAC[1,2], Amandine PALANDRI[2], Amal ZINE EL AABIDINE[3], Thomas MANGEAT[4], Tatiana MERLE[1], Martine CAZALES[1], Antonio TRULLO[2], Christian ROUVIERE[5], Virginia PIMMETT[2], Mounia LAGHA[2]*, Magali SUZANNE[1]*

[1] Molecular, Cellular and Developmental Biology unit (MCD), Centre de Biologie Intégrative (CBI), Université de Toulouse, CNRS, UPS, France

[2] Institut de Génétique de Montpellier, CNRS UMR5535, Univ Montpellier, Montpellier, France

[3] Bioinformatic Facility, Institut de Génétique de Montpellier, CNRS UMR5535, Univ Montpellier, Montpellier, France

[4] LITC Facility, Centre de Biologie Intégrative (CBI), Université de Toulouse, CNRS, UPS, France

[5] Image analysis Facility, Centre de Biologie Intégrative (CBI), Université de Toulouse, CNRS, UPS, France

* corresponding authors: magali.suzanne@utoulouse.fr and mounia.lagha@igmm.cnrs.fr

Abstract

During epithelial-to-mesenchymal transition (EMT), cells undergo profound shape changes and generate mechanical forces. How the nucleus reacts to these mechanical cues, ensuring a tight balance between mechano-protection and mechanotransduction is a key yet unresolved question. Here we show that the transcriptional response to mechanical cues is spatially restricted during EMT. Using *Drosophila* mesoderm invagination as an integrated model of EMT, we quantified single nuclei deformation, nuclear envelope biophysical properties and transcriptional responses during EMT. We found that two conserved pro-EMT genes, *snail (sna)* and *twist (twi)*, respond differently to forces. We show that *twi (*but not *snail)* transcription is enhanced in deformed nuclei, and micromanipulations via optical tweezers is sufficient to rapidly activate *twi* transcription *in vivo*. We further reveal the genome wide response to EMT mechanical forces. Surprisingly mechanosensitive genes seem to be polarized along the nuclear apico-basal axis, revealing a mechanoprotective apical nuclear environment. Direct manipulations of the nuclear envelope in living embryos prove sufficient to induce an immediate transcriptional response, but solely when applied to basal nuclear regions. Overall, these results reveal that EMT nuclei respond directly to forces within seconds and in a regionalized manner.

Introduction

The epithelio-mesenchymal transition (EMT) is a cellular process crucial to form different cell layers during development. Importantly, EMT is also associated with increased drug resistance and invasiveness in cancer (Yang et al. 2020). The transition from epithelial to mesenchymal status notably includes numerous intermediate steps of force generation (Font-Noguera et al. 2021), which coincide with an critical transcriptional shift. Importantly, forces can be sensed by the nucleus. Although nuclear responses to forces have been totally unexplored during EMT, it has been studied in the context of cell differentiation. It was shown that the nucleus can respond to forces in two opposite manners, acting as a shield to protect nuclear content from external mechanical forces (Stephens et al. 2017; Cho et al. 2017) or as a 'transmitter' to convert mechanical stimuli into nuclear biochemical signals, a process known as mechanotransduction (Dupont and Wickström 2022; Maurer and Lammerding 2019). These studies addressed the global nuclear responses to well defined mechanical cues. *in vivo*However**, how the balance between nuclear mechanoprotection and mechanotransduction is established remains largely unexplored in the complex environment of a living organism and totally unknown during EMT.**

The temporal evolution of nuclear responses to mechanical challenges is an open question. Recent work proposed that different responses to mechanical stresses may reflect distinct temporal phases of cellular adaptation (Nava et al. 2020), highlighting the importance of considering temporal resolution in mechanotransduction response. Mechanical forces are transmitted to the nucleus within milliseconds (Wang et al. 2009). This fast transmission constitutes a hallmark of mechanotransduction, operating far more rapidly than any biochemical signaling pathway (Wang et al. 2009; Na et al. 2008). However, nuclear responses to mechanical cues have thus far only been apprehended at the scale of minutes or hours to days (Tajik et al. 2016; Sun et al. 2020; Jian Sun et al. 2023)(Nava et al. 2020; Hsia et al. 2022; Killaars et al. 2019). **Thus, the short-term nuclear response to mechanical challenges remains poorly characterized.**

In this study, **we address how EMT nuclei respond to mechanical cues with an unprecedented spatio-temporal resolution**. We used *Drosophila* mesoderm invagination, a well-established model of EMT. At the onset of EMT, we observed regionalized and stereotyped nuclear deformations coinciding with apical constriction and basal nuclear relocation. By applying compressive stress to living embryos while simultaneously recording transcription, we demonstrated a direct, immediate mechanical response—activating the transcription of *twi* but not *sna*—highlighting distinct mechanosensitivities of these two conserved EMT genes. We next mapped the genome-wide transcriptional landscape of EMT cells using NET-seq and genetic perturbations preventing EMT-associated nuclear deformations. We discovered a spatial bias in nuclear mechanosensitivity, with mechanosensitive genes predominantly located at the basal region of the nucleus. To determine whether this spatial response was purely mechanical, we induced localized deformations of the nuclear envelope in live embryos using optical tweezers as a non-invasive technique. Only basal stimulation triggered a transcriptional response, suggesting a protective mechanism at the apical region of the nucleus. Finally, we tested whether repositioning a non-mechanosensitive gene like *sna* from apical to basal regions could confer mechanosensitivity. Remarkably, basal relocation alone was sufficient to render *sna* promoter responsive to mechanical cues, suggesting the presence of a permissive microenvironment at the basal nuclear region that enables force-dependent transcription. Together, our findings uncover a rapid, spatially patterned transcriptional response to mechanical stress during EMT, orchestrated along the apico-basal nuclear axis.

Results

Nuclei are apically deformed at the onset of EMT

During the various steps constituting the EMT, cells generate different types of forces. In order to investigate how the nucleus responds to this mechanical stress, we quantified nuclear deformations during *Drosophila* mesoderm invagination (aspect ratio, deformation index, see Fig. 1A-E and Methods).

Prior to mesoderm invagination and associated EMT, nuclei exhibit a regular and elongated shape along the apico-basal axis (Fig. 1A). In contrast, during invagination, apical deformations are detected as concave domains (Fig. 1A-B). When comparing nuclei pre-EMT (cellularization) or during EMT (invagination), clear differences in aspect ratios and deformation indexes emerge (Fig. S1A-B). Interestingly, these deformations seem restricted to the apical part of the nuclei as illustrated in 3D reconstructions and transverse sections (Fig. 1A). Moreover, they are more prevalent in the mesoderm compared to lateral and dorsal regions (Fig. S1C-E). Collectively, these results show that invaginating nuclei become apically deformed during EMT.

When quantifying nuclear deformations within the invaginating mesoderm, we noticed an important inter-nuclear variability (Fig. 1A). This prompted us to analyze nuclear shape at a single nucleus level, using the distance from the apical surface of the embryo (depth) as a proxy of EMT progression (Fig. S1F-H). We found that the percentage of deformed nuclei increases with depth (Fig. S1H), indicating that deformations become more frequent as nuclei relocate basally. This analysis revealed a temporal correlation between apical nuclear deformation and basal repositioning.

Perturbing nuclear stiffness is sufficient to impair EMT nuclear deformations

The emergence of nuclear deformations indicates a change in the balance of forces acting on the nucleus. At the onset of EMT, apical constriction has been proposed to create a cytoplasmic flow responsible for nuclear relocation from apical to basal (Gelbart et al. 2012). This flow is likely involved in apical deformations. We hypothesized that the observed deformations could be further facilitated by a decrease in nuclear envelope mechanical resistance. To test this, we quantified nuclear rigidity over time using optical tweezers. Contrary to other methods such as atomic force microscopy (AFM) or magnetic tweezers, optical tweezers are non-invasive and are uniquely capable of measuring nuclear stiffness *in vivo* in living embryos. By trapping lipid droplets (naturally present in the embryo and used as internal probes), we locally indented a target nucleus and determined the physical properties of the nuclear envelope (see Fig. 1F, and Fig. 1G for a schematic representation). Interestingly, we found that nuclei were significantly softer at the onset of EMT (beginning of invagination) compared to 10 minutes prior (during late cellularization) (Fig. 1H), revealing temporal changes in nuclei viscoelasticity at the onset of EMT. We next measured the relaxation dynamics of the induced nuclear deformations. Regardless of the stage examined, nuclei returned to their original shape within a few seconds (Fig. 1I).

Since nuclear softening coincides with nuclear deformation, we reasoned that changing the stiffness of nucleus during EMT could impact force transmission. To test this hypothesis, we used mutant for *kugelkern* (*kuk*), which encodes a nuclear lamina protein that modulates nuclear rigidity (Hampoelz et al., 2011). We first characterized how nuclear stiffness evolves at the onset of EMT in *kuk* hypomorphic mutant ($kuk^{EY07696}$) living embryos. We found the nuclear envelope less deformable

in *kuk* mutants compared to the control, showing no clear indentation even when stronger force was applied with optical tweezers (Fig. 1F'-F''). Consistently, nuclear envelope stiffness was significantly increased in *kuk* mutants, both before and at the onset of EMT (Fig. 1H), while relaxation dynamics was similar to the control (Fig. 1I). We conclude that *kuk* mutant nuclei are significantly more rigid than their wild type counterparts, both before and during EMT. We next analyzed nuclear shape in *kuk* mutants. Interestingly, we found that nuclei are rounder and apical deformations are largely absent in *kuk* mutants (Fig. 1C-E). Given the absence of nuclear deformation in the *kuk* mutant, this genetic background represents an ideal context for investigating the loss of force transmission to the nucleus.

Gradual and immediate response of *twist* to mechanical challenges during EMT

Having identified a mutant context abolishing nuclear deformation and thus impairing force transmission to the nucleus, we next explored how the absence of apical deformations affects transcriptional states during EMT. We focused on *sna* and *twi,* two conserved genes orchestrating various EMT steps including mesoderm invagination. In *Drosophila* embryos, prior works using static approaches suggested that cytoplasmic mRNA levels of *twi* and *sna* were sensitive to mechanical cues (Farge 2003; Desprat et al. 2008). We therefore sought to test whether the nascent transcription of *sna* and *twi* could potentially respond to EMT-generated forces.

To quantify how *sna* and *twi* transcription evolves upon nuclear deformation, two metrics were scored: the number of active transcriptional site (TS) per nucleus or transcriptional activation and the sum of TS intensity per nucleus or transcriptional level. In wild type embryos, we did not detect obvious differences in *sna* transcription between deformed and undeformed nuclei (Fig. 2A, C-D). In contrast, *twi* transcription was significantly increased in deformed nuclei, both in terms of transcriptional activation and transcriptional level per nucleus (Fig. 2A', C'-D'). This indicates that an increase in *twi* transcription coincides with nuclear deformation during EMT, while *sna* transcription remains unchanged upon deformation.

When nuclear force transmission is impaired in *kuk* mutants, *sna* transcriptional activation is unaffected (Fig. 2C-D). This is not the case for *twi* transcription, in which a significant decrease in transcriptional activation is observed in *kuk* mutants (Fig. 2C'-D'). However, transcriptional levels are reduced for both *sna* and *twi* in this mutant context (Fig. 2D-D'). Thus, both *sna* and *twi* transcription is modified in the absence of nuclear deformations, albeit differently, suggesting that different mechanisms may be at play.

Next, we sought to test whether the direct application of mechanical forces was sufficient to affect *twi* and *sna* nascent transcription. We applied manual compression to living embryos while monitoring transcriptional activity in real time using the MS2/MCP system (Fig. 2E). For each experiment, the nuclear aspect ratio was used as a readout for the level of compression applied (Fig. S2). Importantly, the induced nuclear deformation was slightly higher but of the same order of magnitude as that observed during natural mesoderm invagination (Fig. 2F). Endogenous *sna* and *twi* transcription dynamics were monitored using MS2 knock-in lines (Pimmett et al. 2025). Upon compression, *sna* nascent transcription remained stable (Fig. 2G-H), independently of the level of compression applied (Fig. 2I). This demonstrates that *sna* transcription is not directly responsive to mechanical forces, at least in the range of forces applied in this experiment. In contrast, compression triggered a rapid and substantial increase (~ 40%) in *twi* transcriptional activity (Fig. 2G'-H'). The intensity of transcriptional activation correlated linearly with the extent of nuclear deformation, indicating that greater nuclear deformation elicits a stronger Twi transcriptional response (Fig. 2I').

These results also revealed a surprisingly rapid (seconds) transcriptional response to force application (Fig. 2H').

Taken together, these results indicate that although *sna* transcription is altered in *kuk* mutants—where force transmission to the nucleus is impaired—it does not respond to the direct application of mechanical forces in an embryo undergoing compression. However, *twi* transcription does respond directly to mechanical forces as shown by (1) the increase in *twi* transcription in deformed nuclei, (2) the decrease of *twi* transcription in *kuk* mutants where nuclear deformations are impaired and (3) the increase in *twi* transcription in response to compression.

Monitoring nascent transcription upon compression in living embryos revealed an unexpected distinct response for *sna* and *twi*: *sna*, located apically near the deformed area, shows little or no direct response to mechanical forces, while *twi*, positioned basally, displays a rapid and gradual response. Given that these two loci are located in separate regions of the nucleus (Dufourt et al. 2021)(Fig. 2B-B'), we reasoned that their nuclear positioning could be responsible for their differential response to mechanical stimuli. To investigate the effect of nuclear positioning on mechanical response, we basally relocated an apical gene and quantified it response to forces. We used a transgenic line in which the regulatory region of *sna* followed by a yellow-MS2 cassette was inserted in a genomic region closer to the *twi* locus and thus more basally within the nucleus (Bothma et al. 2015a). Interestingly, the *sna*-yellow-MS2 cassette exhibited a rapid yet gradual transcriptional response to compressive forces, similar to that observed for *twi* (compare Fig. 2G''-I'' to Fig. 2G'-I'). This indicates that shifting *sna* from an apical to a basal region, is sufficient to confer mechanosensitivity, supporting our hypothesis that a mechanosensitive transcriptional response depends on the nuclear positioning of a given gene.

Genome wide response to EMT mechanical forces is regionalized

To investigate if EMT nuclei indeed exbibit a regionalized response to forces, we employed a genome-wide approach using nascent RNA sequencing (NET-seq). In brief, NET-seq is based on the isolation of transcription complexes formed by Pol II, the DNA template and nascent RNA through immunoprecipitation (IP) of an elongation-specific form of RNA Pol II (Prudêncio et al. 2022). specifically capturing nascent RNA transcripts (in the process of being synthesized). NET-seq was performed in wild type and *kuk* mutant embryos in which nuclear envelope deformation and force transmission are impaired, at two developmental stages: during cellularization, just before EMT (2h-2h30 AEL), and during gastrulation, when EMT forces are active (3h-3h30 AEL). We first validated the NET-seq data by confirming the presence of ubiquitously expressed genes (Fig. S3A), the absence of maternal genes (Fig. S3B) and the presence of snRNAs associated with the Pol II complex (Fig. S3C). We further observed a reduction of *kuk* transcripts in *kuk* mutants as expected (Fig. S3D).

We then compared nascent transcripts differing between wild type and *kuk* mutants before the generation of EMT forces (cellularization stage). This small set of transcripts (87) may correspond to loci potentially impacted by the nuclear rigidity defects observed in *kuk* mutants (Fig. 3A). At the later stage, during EMT, a larger number of genes (854) were differentially expressed between the two genetic contexts (Fig. 3B). To focus on genes potentially responding to EMT forces, we subtracted from this list those whose expression varied before any EMT forces are applied. This left us with a list of 833 genes (Fig. 3C). We then further narrowed our selection by conserving genes expressed in the mesoderm (based on RNAseq data, (Jingjing Sun et al. 2023; Ing-Simmons et al. 2021; Calderon et al. 2022)), capturing 91 putative mechanosensitive genes during mesoderm invagination. Interestingly, these genes are mostly repressed during EMT in wild-type embryos, but upregulated in *kuk* mutants (Fig. 3D). We note that *sna* and *twi* are not significantly enriched in this list of genes, although

expressed and detected (Fig. S3D). Differential expression between *kuk* and control conditions is detected, albeit not reaching a statistically significant threshold. This might be due to low coverage of these loci due to their short size.

We next asked whether the identified putative mechanosensitive genes showed a particular distribution within the nucleus. In many cell types, interphase chromosomes exhibit a Rabl organization, whereby centromeres and telomeres cluster at opposite nuclear poles (Comings 1980). This stereotypical chromosomal organization has been well described for the *Drosophila* second chromosome (2L arm)(Marshall et al. 1996). Consistently, we observed a strong correlation between the position of genes along the apico-basal axis of the nucleus (using the TS from smiFISH as a proxy for gene position) and the gene distance from the centromere (Fig. 3F).

Based on the Rabl configuration, we inferred the apico-basal position of all candidate mechanosensitive genes identified with the NET-seq experiment on chromosome II and III (705 of 833 genes). No obvious apico-basal bias was observed (Fig. 3G). However, when we examined more precisely the subset of chromosome II and III genes potentially responding to EMT forces (73 genes from the mesoderm), they appeared largely absent from the apical-most region (Fig. 3H).

These results suggest that the apical region of EMT nuclei may be less responsive to mechanical forces or better protected from them, while the basal region appears more sensitive or less shielded. Altogether, these findings point to a spatially polarized mechanical response in EMT nuclei.

Controlled nanoindentations applied on the nucleus of living embryos is sufficient to induce the transcriptional response of *twist*

To understand the unexpected link between a polarized apical nuclear deformation and a basally-located transcriptional response, we first characterized the volume and shape of nuclear envelope. We found that while the volume remains constant independently of the deformation (Fig. S4A), the nuclear contents are displaced basally, as shown by an increased basal diameter (Fig. S4B-C). This indicates that the apical deformation has a long-range influence.

We next asked whether a local mechanical stress at the basal part of the nuclear envelope would be sufficient to impact gene transcription during EMT. To test this, we used optical tweezer as a non-invasive method to apply a local indentation at different levels along the apico-basal axis of the nuclear envelope (schematized in Fig. 4A-B). To monitor the transcriptional response in real time, this approach was coupled to the MS2/MCP labeling system and live imaging. We first followed the response of *twi* to local indentations generated on the basal region of the nuclear envelope at the level of the *twi* locus (at about 8 µm from the apical surface of the nucleus). Such indentations resulted in a rapid and significant increase in transcriptional signal observed within 8-10 seconds after applying the local force, indicating that a direct mechanical perturbation of the nuclear envelope was sufficient to stimulate *twi* transcription in *Drosophila* embryos. Importantly, this response was strictly local: only TS located within ~2.5 µm of the indentation showed increased transcription, while more distant TS remained unaffected (Fig. 4C-D). In contrast, performing the same experiment on the apical part of the nuclear envelope, at the level of the *sna* locus failed to induce any change in *sna* transcriptional activity, regardless of the distance between the indentation and the TS (Fig. 4C'-D'). Our findings indicate that mechanical forces applied to the nuclear envelope trigger a transcriptional response *in vivo*, but only when delivered basally. Together, these micromanipulations demonstrate that EMT nuclei exhibit a spatially regionalized mechanical response.

Discussion

Cells and tissues are constantly generating and responding to forces. These forces are ultimately decoded at the level of nuclei, where a fine balance between mechanotransduction and mechanoprotection occurs. Understanding how nuclei control this balance, particularly during important cellular transitions such as EMT is a fundamental question. Here we combined imaging and genomics approaches to probe how this occurs in the context of *Drosophila* embryonic gastrulation, where mesoderm nuclei experience a collective EMT. By tracking transcription dynamics concomitantly to micro-manipulating specific regions of EMT nuclei in living embryos, we unveiled important features of nuclear EMT mechanics:

(1) during EMT, nuclear envelope deformations are regionalized; (2) the transcriptional response to forces is spatially restricted during EMT; (3) loci located close to the deformations are mechanoprotected; (4) the transcriptional response to forces occurs within seconds. Overall, our quantitative measurements bring important new insights into how protection and transduction cooperate to orchestrate a specific transcriptional program.

During mesoderm invagination, EMT nuclei exhibit stereotyped and polarized deformations. Our findings indicate a causal link between these polarized deformations and transcriptional response to forces. However, surprisingly, genes located close to the deformed regions are not those responding the most. Genes located in the apical region are protected from mechanotransducive cues, while basally positioned genes are more sensitive to mechanical stimulus. These data reveal a macroscopic regionalization of nuclear mechanics.

Given the absence of mechanical response of apically located genes, we hypothesize that the apical nuclear environment may play a protective role. Precise molecular or biophysical mechanisms ensuring this potential mechanoprotection remain to be elucidated *in vivo* but a few possibilities can be hypothesized.

Apical mechanoprotection may rely on a particular nuclear organization with a polarized chromatin organization. In all eukaryotic genomes, heterochromatin represents a distinct nuclear domain, often located in specific regions like the nuclear periphery, and organized as pericentromeric bodies or chromocentres. However, exceptions such as mouse rod photoreceptor nuclei exist, where heterochromatin is located centrally (via a unique large chromocenter), surrounded by peripheral euchromatin (Solovei et al. 2009), referred to as 'inside-out nuclei'. In other species, chromosomes follow a Rabl configuration whereby centromeres and telomeres cluster at opposite nuclear poles (Comings 1980; Marshall et al. 1996), such as the apical positioning of heterochromatin in *Drosophila* embryos. Interestingly, we noticed enhanced enrichment of apical heterochromatin upon deformation (Fig. S4E-F). Since this Rabl organization is prevalent in different species, it is tempting to speculate that the polarized response observed in *Drosophila* embryos could be broadly generalizable. It would be interesting to examine whether nuclear polarization is a general feature of EMT and how mechanical response to deformation is conserved.

Additionally, nuclear deformation results in increased enrichment of LaminDm0 at the apical region of *Drosophila* EMT nuclei (Fig. S4D). These observations suggest a structural reinforcement of the nucleoskeleton in the apical region during EMT. The combination of an augmented nucleoskeleton and chromatin condensation could create an apical mechanical shield, protecting the apical part of the nucleus from EMT forces and imposing distinct constraints along the apico-basal axis. A crowded apical environment may restrict chromatin mobility and diminish the probability of enhancer-promoter contact. In contrast, genes positioned basally may benefit from an increased chromatin mobility,

increasing the likelihood of productive enhancer-promoter contacts. Our discovery of a differential mechanical response along the apico-basal axis opens interesting avenues for other cellular contexts where chromatin is differentially organized, such as the mouse retina, where regionalized transcriptional responses could also occur. Our measurements indicate that nuclear response to mechanical input is extremely rapid. While mechanical force transmission only takes a few milliseconds, the nuclear mechanical response has thus far only been quantified after several minutes or even hours. Here, the direct micromanipulation of the nuclear envelope coupled to nascent mRNA labeling in a living embryo allowed us to reveal that a transcriptional response takes no more than a few seconds. Given this timescale, we can speculate on possible underlying mechanisms and exclude those operating at longer timings, such as nuclear import of a transcription factor, as shown for YAP, allowed by nuclear pore opening upon a mechanical stimulus (Elosegui-Artola et al. 2017). Another described mechanism of mechanotransduction that could intuitively fit with the observed timing is the direct impact of forces on chromatin stretching (Tajik et al. 2016). However, since mechanosensitive loci are primarily located far from the nuclear deformation, we disfavor chromatin stretching as a potential mechanism. Instead, we postulate that the spatially restricted transcriptional response observed could be due to the relocation of a targeted locus to a more favorable environment, where Pol II and other transcription drivers are more abundant. Future studies testing the existence of mechanosensitive transcriptional hubs in specific regions of the nucleus or the formation of mechanoresponsive nuclear condensates following stress may prove enlightening.

In conclusion, our work unmasks spatial heterogeneity in nuclear mechanics. Looking ahead, we anticipate that this finding, along with the quantitative imaging framework we developed, will set the foundation to dissect nuclear mechanisms of other EMTs, including in disease contexts.

Acknowledgements: We are grateful to Pedro António Pereira Prudêncio and Carmo Fonseca for sharing their expertise in Drosophila Net-seq experiments. We thank Cyril Esnault for advice in Net-seq experiments. We thank Hiroshi Kimura for sharing Pol II antibodies. We thank Corinne Benassayag for constructive comments on the manuscript. We acknowledge the Bioinformatics platform BigA, the Imaging platform LITC and the Drosophila facility from the CBI, the Montpellier Ressources Imagerie facility (France-BioImaging) and the Biocampus Drosophila facility of Montpellier. MS's research is supported by the Center National de la Recherche Scientifique (CNRS), the University of Toulouse and funded by grants from the National Agency of Research (ANR, PRC AAPG2021, CellPhy), the Research Association against Cancer (ARC, Programme Labélisé AAP2020, ARCPGA12020010001154_1591) and the Medical Research Fundation (FRM, Equipes FRM, EQU202403018134). Research in the laboratory of M.L. is supported by the Center National de la Recherche Scientifique (CNRS), the University of Montpellier and is funded by grants from the Fondation Bettencourt Schueller, the European Molecular Biology Organization Young Investigator program (EMBO YIP), ERC (LightRNA2Prot), and ANR CellPhy. M.L and A.T. are sponsored by the CNRS.

Author's contributions: Conceptualization: M.S and M.L; **Formal analysis:** R.B, A.P, A.Z, Thomas Mangeat (TM1), TM2; AT; C.R. **Investigation**: R.B, A.P, TM1, C.R, V.P. **Writing – Original Draft**: R.B.,

M.S and M.L; **Writing-Editing**: R.B., M.S and M.L; **Visualization**: R.B; **Supervision**: M.S and ML; **Resources**: V.P; **Project administration**: M.S and M.L; **Funding acquisition**: M.S and M.L.

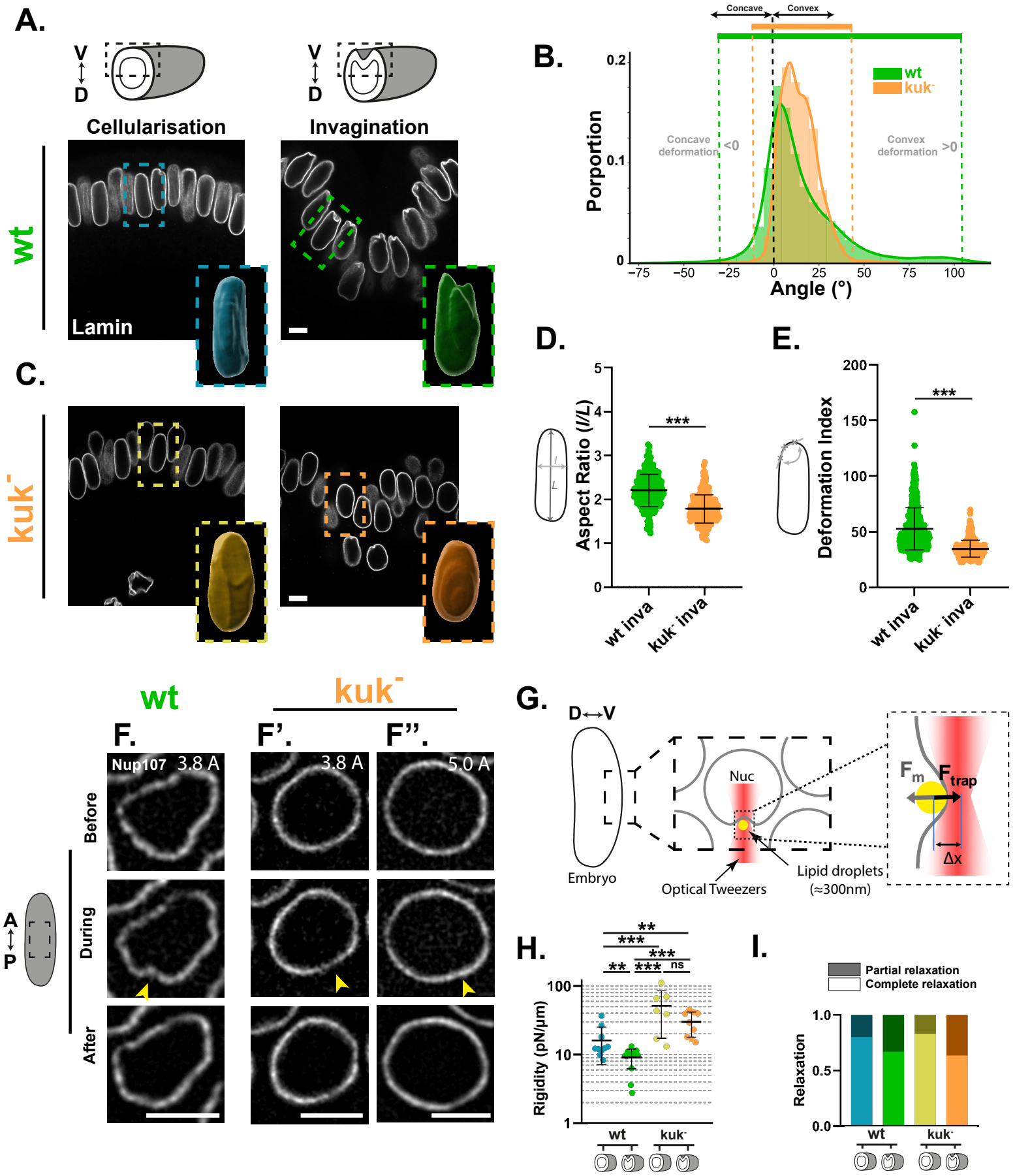
A.
V
D
Cellularisation
Invagination
wt
Lamin
C.
kuk-
B.
Concave
Convex
wt
kuk-
Concave deformation <0
Convex deformation >0
Porportion
Angle (°)
D.
Aspect Ratio (l/L)
***
wt inva
kuk- inva
E.
Deformation Index
***
wt inva
kuk- inva
wt
kuk-
F.
F'.
F''.
Nup107 3.8 A
3.8 A
5.0 A
Before
During
After
A
P
G.
D↔V
Embryo
Nuc
Optical Tweezers
Lipid droplets
(≈300nm)
Fm
Ftrap
Δx
H.
Rigidity (pN/µm)
wt
kuk-
I.
Partial relaxation
Complete relaxation
Relaxation
wt
kuk-

Figure 1: Nuclei undergo stereotyped deformation during EMT: A. Transverse sections of embryos stained for LaminDm0 showing nuclear morphology in wild-type (wt) embryos during cellularization (pre-EMT, left) and invagination (EMT, right). Selected nucleus (indicated by a dashed-line square) was reconstructed in 3D and shown in the inset on the right. B. Distribution of curvature angles along the apical region of the nuclear envelope in wt and *kuk* mutants (wt: N=4, n=215; *kuk*: N=3, n=128) during EMT. The black dashed line separates convex deformations (angle > 0) from concave ones (angle < 0). C. Transverse sections stained for LaminDm0 showing nuclear morphology of *kuk* mutant embryos during cellularization (pre-EMT, left) and invagination (EMT, right). Selected nucleus (indicated by a dashed-line square) was reconstructed in 3D and shown in the inset on the right. D. Quantification of nuclear aspect ratio during gastrulation in wt and *kuk* mutants (wt: N=8, n=431; *kuk*: N=7, n=292). E. Nuclear deformation index measured in wt and *kuk* mutant embryos during EMT (wt: N=8, n=431; *kuk*: N=7, n=292). F. Time-lapse snapshots from optical tweezer experiments showing 3 successive time points: before-indentation (calibration, top), during indentation (measurement, middle), and after-indentation (relaxation, bottom), in wt nuclei at 3.8 A (F), *kuk* mutants at 3.8 A (F'), and *kuk* mutants at 5 A (F''). G. Schematic representation of the optical tweezer method. H. Quantification of nuclear rigidity measured by optical tweezers in wt and *kuk* mutants, 10 minutes before and at the onset of EMT (wt: N=8, n1=11, n2=15; *kuk*: N=7, n1=11, n2=15). I. Quantification of relaxation dynamics from optical tweezer experiments for the same conditions as in G (wt: N=8, n1=11, n2=15; *kuk*: N=7, n1=11, n2=15). Statistical significance was assessed by the Mann−Whitney test (Fig. 1D&G), Kolmogorov-Smirnov test (Fig1. E), (*****=p<0,05; ******=p<0,01; *******=p<0,001). Scale bar = 5 µm

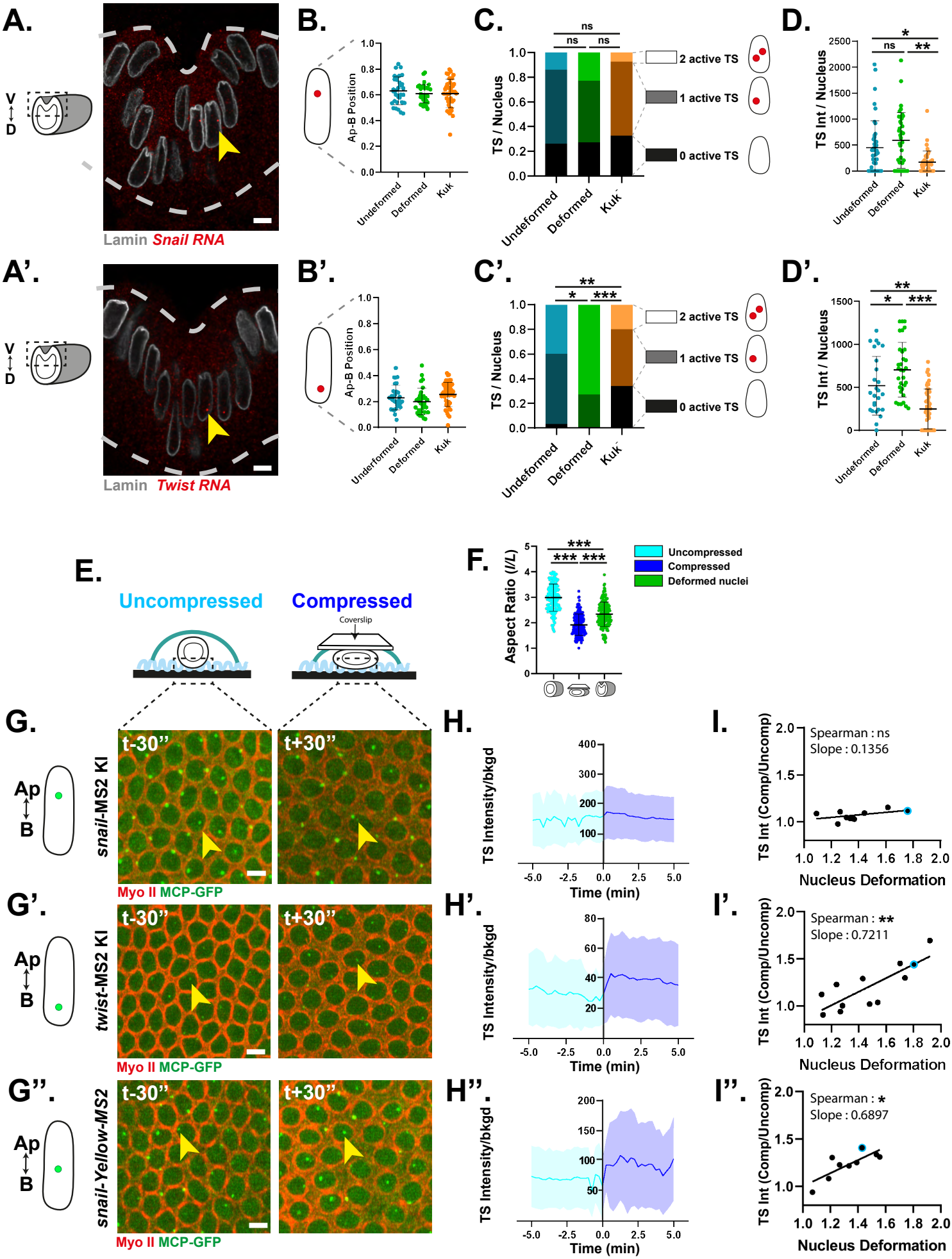
A.
V
D
Lamin Snail RNA
B.
Ap-B Position
Undeformed
Deformed
Kuk
C.
ns
ns
ns
TS / Nucleus
2 active TS
1 active TS
0 active TS
Undeformed
Deformed
Kuk
D.
*
ns
**
TS Int / Nucleus
Undeformed
Deformed
Kuk
A'.
V
D
Lamin Twist RNA
B'.
Ap-B Position
Undeformed
Deformed
Kuk
C'.
**
*
***
TS / Nucleus
2 active TS
1 active TS
0 active TS
Undeformed
Deformed
Kuk
D'.
**
*
***
TS Int / Nucleus
Undeformed
Deformed
Kuk
E.
Uncompressed
Compressed
Coverslip
F.
***
***
***
Aspect Ratio (l/L)
Uncompressed
Compressed
Deformed nuclei
G.
Ap
B
snail-MS2 KI
t-30"
t+30"
Myo II MCP-GFP
G'.
Ap
B
twist-MS2 KI
t-30"
t+30"
Myo II MCP-GFP
G''.
Ap
B
snail-Yellow-MS2
t-30"
t+30"
Myo II MCP-GFP
H.
TS Intensity/bkgd
Time (min)
H'.
TS Intensity/bkgd
Time (min)
H''.
TS Intensity/bkgd
Time (min)
I.
Spearman : ns
Slope : 0.1356
TS Int (Comp/Uncomp)
Nucleus Deformation
I'.
Spearman : **
Slope : 0.7211
TS Int (Comp/Uncomp)
Nucleus Deformation
I''.
Spearman : *
Slope : 0.6897
TS Int (Comp/Uncomp)
Nucleus Deformation

Figure 2: Mechanosensitive transcription of *snail* and *twist* depends on their nuclear localization: A. Transverse sections of embryos stained for LaminDm0 and hybridized via smiFISH for *snail* (A) or *twist* (A'). Dashed lines indicate the apical and basal sides of the tissue. B. Quantification of the spatial position of *snail* (B) or *twist* (B') TS in undeformed, deformed, and *kuk* mutant nuclei (*snail*: undeformed: N=3, n=32; deformed: N=3, n=43; *kuk*: N=4, n=40; *twist*: undeformed: N=3, n=30; deformed: N=3, n=30; *kuk*: N=5, n=50). C. Quantification of the number of TS per nucleus for *snail* (C) and *twist* (C') in undeformed, deformed, and *kuk* mutant nuclei (for *snail*: wt N=8, n=80; *kuk* N=4, n=40; for *twist*: wt N=6, n=60; *kuk* N=5, n=50). D-D'. Quantification of the normalized total TS intensity per nucleus for *snail* (D) and *twist* (D') in undeformed, deformed, and *kuk* mutant nuclei (for *snail*: wt N=8, n=80; *kuk* N=4, n=40; for *twist*: wt N=6, n=60; *kuk* N=5, n=50). E. Schematic representation of the mechanical compression setup. For details of quantification methods, see FigS3. F. Quantification of nuclear aspect ratio before and after compression, compared with deformed nuclei in control embryos (before/after compression: N=17 n=170, deformed: N=8, n=190). G-G'-G''. Time-lapse snapshots from the compression experiment taken before (left) and after (right) compression for *snail*-MS2 KI (G), *twist*-MS2 KI (G'), and the transgenic snail reporter line insert in basal (snail-Yellow-MS2 Bac) (G''). Yellow arrows indicate the same transcription site before and after compression. MyoII is shown in red, MCP-eGFP (TS) in green. H. Representative curves of mean normalized TS intensities over time during compression of *snail*-MS2 KI (H), *twist*-MS2 KI (H'), and basal snail-Yellow-MS2 (H'') embryos. Light blue indicates before compression, dark blue after compression. The dashed line marks the frame at which compression was applied (t0). I. Correlation between variation in TS intensity (ratio before vs after compression) and nuclear deformation (nuclear aspect ratio variation see Fig.S2) in *snail*-MS2 KI (I), *twist*-MS2 KI (I'), and basal snail-Yellow-MS2 (I'') embryos (N=9, 12, and 9, respectively). Statistical analyses: Mann–Whitney test (Fig. 2D&F), Fisher's exact test (Fig. 2C), and Spearman's rank correlation (Fig. 2H) ($p<0.05$ =*; $p<0.01$=**; $p<0.001$=***). Scale bar = 5 µm

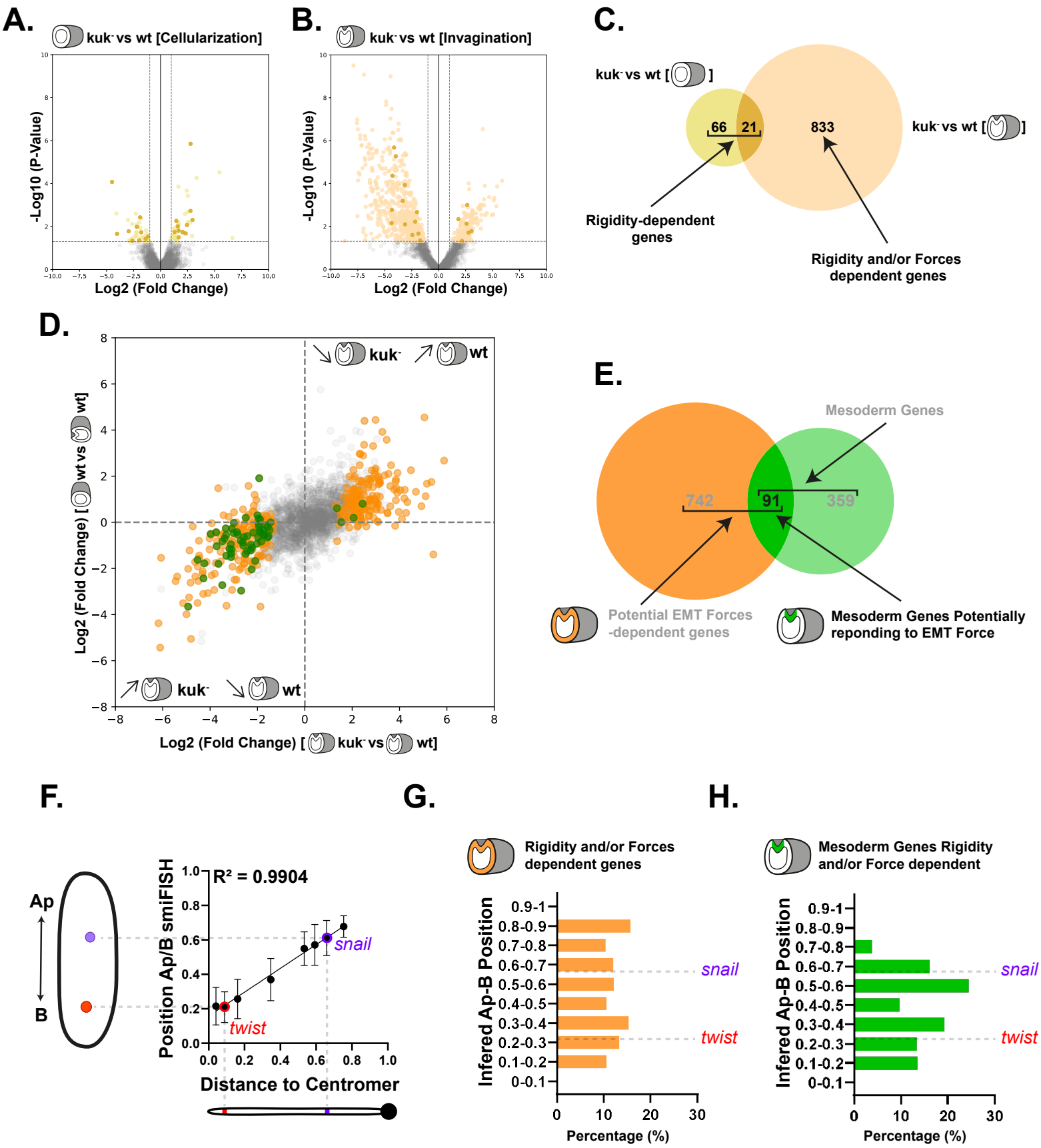
A.
kuk⁻ vs wt [Cellularization]
-Log10 (P-Value)
Log2 (Fold Change)
B.
kuk⁻ vs wt [Invagination]
-Log10 (P-Value)
Log2 (Fold Change)
C.
kuk⁻ vs wt [ ]
66
21
833
kuk⁻ vs wt [ ]
Rigidity-dependent genes
Rigidity and/or Forces dependent genes
D.
kuk⁻
wt
kuk⁻
wt
Log2 (Fold Change) [wt vs wt]
Log2 (Fold Change) [kuk⁻ vs wt]
E.
Mesoderm Genes
742
91
359
Potential EMT Forces -dependent genes
Mesoderm Genes Potentially reponding to EMT Force
F.
Ap
B
R² = 0.9904
snail
twist
Position Ap/B smiFISH
Distance to Centromer
G.
Rigidity and/or Forces dependent genes
Infered Ap-B Position
0.9-1
0.8-0.9
0.7-0.8
0.6-0.7
0.5-0.6
0.4-0.5
0.3-0.4
0.2-0.3
0.1-0.2
0-0.1
snail
twist
Percentage (%)
H.
Mesoderm Genes Rigidity and/or Force dependent
Infered Ap-B Position
snail
twist
Percentage (%)

Figure 3: Mechanosensitive genes are depleted from the apical, deformed nuclear region: A-B. Volcano plots showing differentially expressed genes between wt and *kuk* mutant embryos during cellularization (A, before EMT) and during EMT (B). C. Venn diagram comparing the sets of differentially expressed genes identified in panels A and B. The bracket corresponds to genes potentially regulated by nuclear rigidity alone; on the right, 833 genes may respond to mechanical forces. D. Scatter plot showing the correlation between the log2 fold change of genes during wt gastrulation (y-axis) and the log2 fold change between wt and *kuk* mutant during EMT (x-axis). **E.** Venn diagram identifying, from the set of 833 force-responsive genes identified in C, those also expressed in the mesodermal region genes based previous studies (Jingjing Sun et al. 2023; Ing-Simmons et al. 2021; Calderon et al. 2022). F. Correlation between gene positioning along the apico-basal axis of the nucleus (from smiFISH see *Methods*) and their genomic distance to the centromere. *snail* (violet), which localizes apically, is closer to the centromere than *twist* (red), which is basally localized. G-H. Distribution of potentially mechanosensitive genes from chromosome II and III based on their inferred nuclear positioning along the apico-basal axis, derived from their centromeric distance using the correlation in panel F. Bar plot shows the proportion of all mechanosensitive genes (G) or mechanosensitive genes from the mesoderm (H) within each nuclear region.

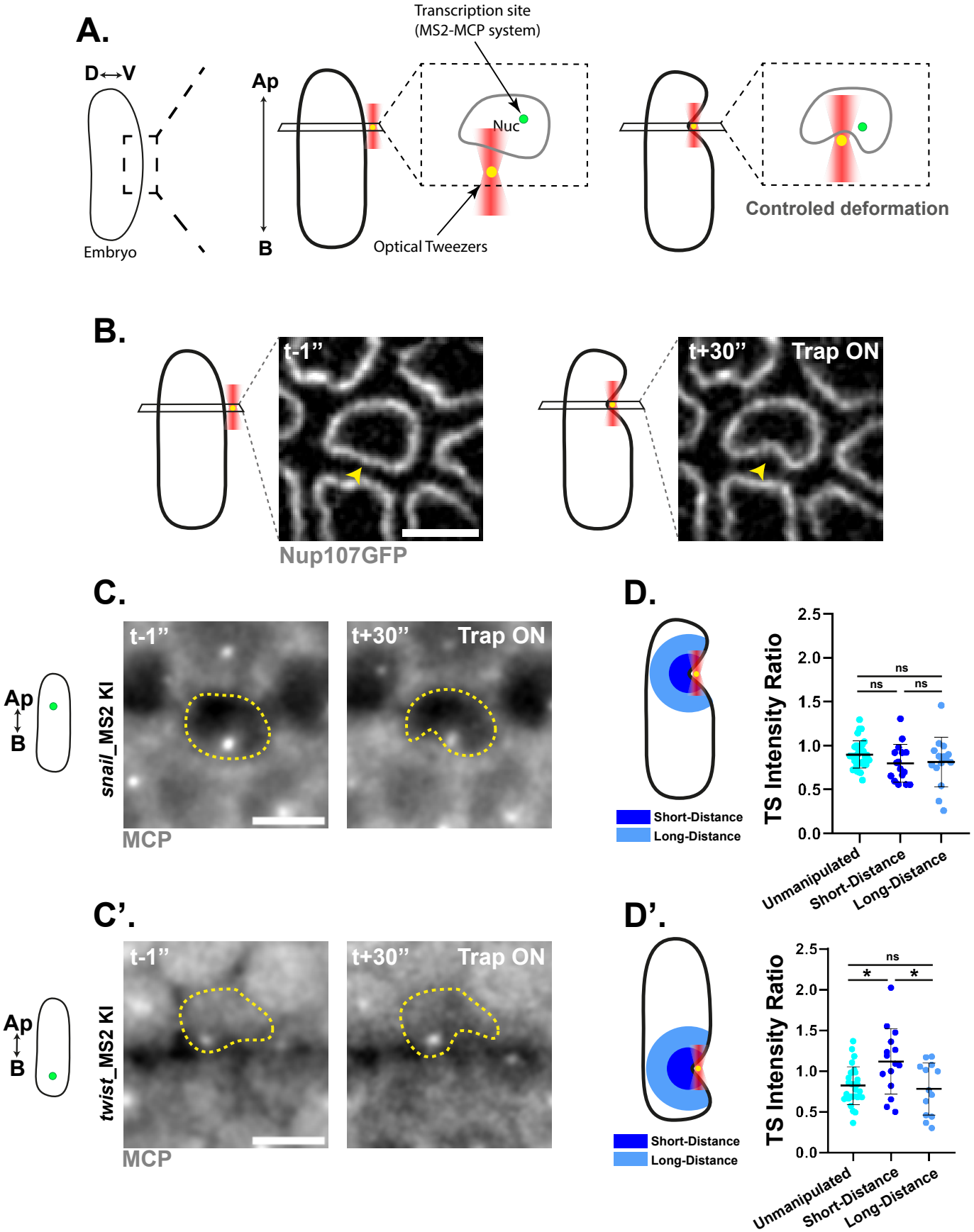
A.
D↔V
Embryo
Ap
B
Transcription site
(MS2-MCP system)
Nuc
Optical Tweezers
Controled deformation
B.
t-1”
t+30”
Trap ON
Nup107GFP
C.
Ap
B
snail_MS2 KI
t-1”
t+30”
Trap ON
MCP
D.
Short-Distance
Long-Distance
TS Intensity Ratio
2.5
2.0
1.5
1.0
0.5
0.0
ns
ns
ns
Unmanipulated
Short-Distance
Long-Distance
C’.
Ap
B
twist_MS2 KI
t-1”
t+30”
Trap ON
MCP
D’.
Short-Distance
Long-Distance
TS Intensity Ratio
2.5
2.0
1.5
1.0
0.5
0.0
ns
*
*
Unmanipulated
Short-Distance
Long-Distance

Figure 4: Local nuclear deformation is sufficient to trigger rapid and regionalized transcriptional response: A. Schematic representation of the experimental setup allowing controlled deformation of nuclei while monitoring transcription using the MS2-MCP system. B. Schematic representation of the experiment, along with representative snapshots extracted from a timelapse, following the nuclear envelope (Nup107-GFP) before (left) and during (right) localized nuclear deformation using optical tweezers. The yellow arrow indicates the initial position of trap. C. Representative images from live MS2/MCP experiments showing TS before (left) and during (right) localized nuclear deformation. C: *snail-MS2* KI; C': *twist-MS2* KI. Yellow dashed lines indicate the estimated nuclear boundaries, based on brightfield images (data not shown). D. Schematic representation of the quantification method. TS located within 2.5 µm of the trap initial position are classified as "short distance", while those further away are "long distance" (left). Quantification of the change in TS intensity before and after local deformation (right). Control TS are unmanipulated nuclei adjacent to the manipulated one. D: *snail-MS2* KI; D': *twist-MS2* KI (*snail*: N=7, n=33; *twist*: N=12, n=28). Statistical significance was assessed by the Mann−Whitney test (*****= p<0,05; ******=p<0,01; *******=p<0,001). Scale bar = 5 µm

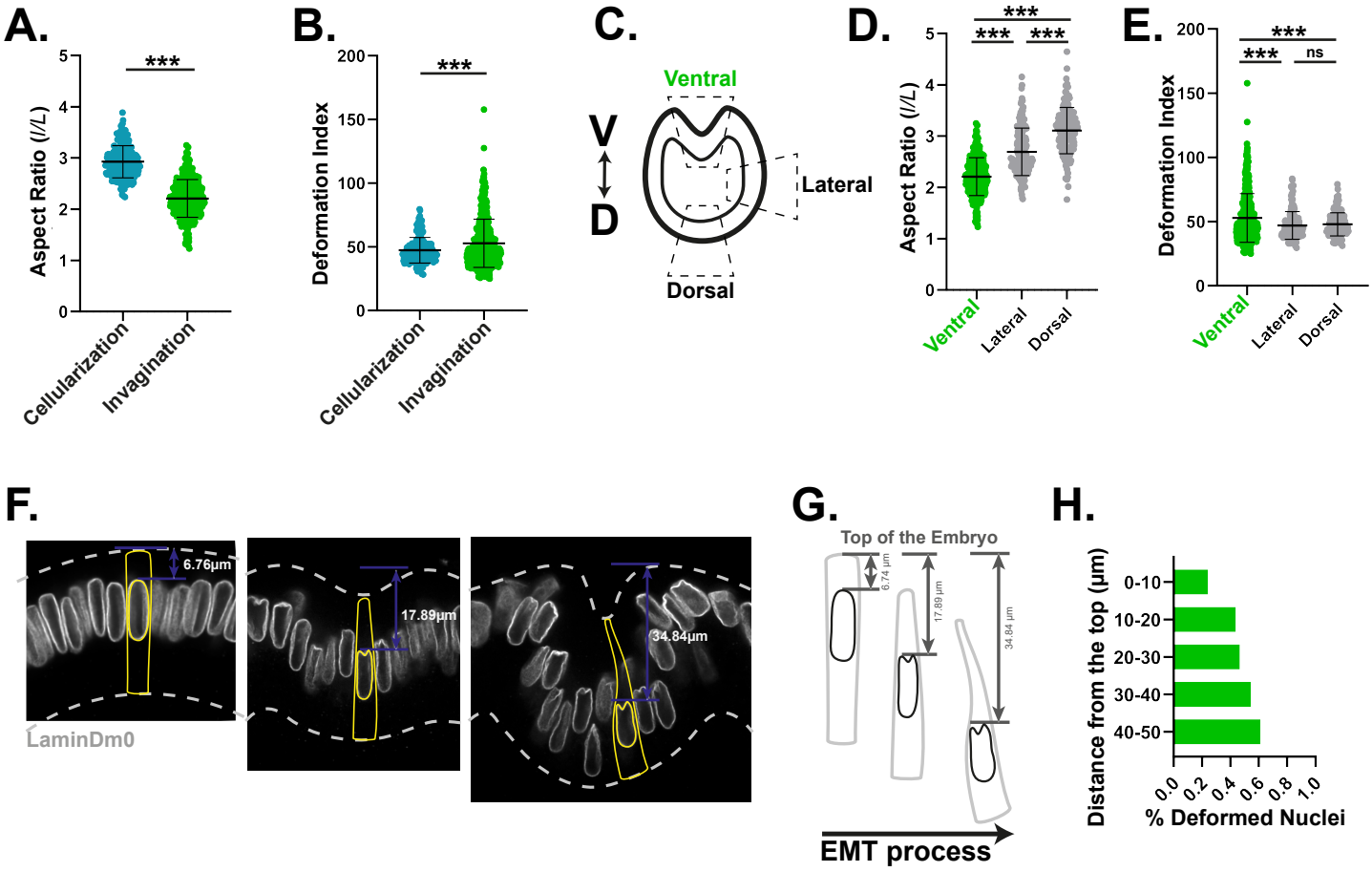
A.
Aspect Ratio (l/L)
***
Cellularization
Invagination
B.
Deformation Index
***
Cellularization
Invagination
C.
Ventral
V
D
Lateral
Dorsal
D.
Aspect Ratio (l/L)
***
***
***
Ventral
Lateral
Dorsal
E.
Deformation Index
***
***
ns
Ventral
Lateral
Dorsal
F.
6.76µm
17.89µm
34.84µm
LaminDm0
G.
Top of the Embryo
6.74 µm
17.89 µm
34.84 µm
EMT process
H.
Distance from the top (µm)
0-10
10-20
20-30
30-40
40-50
% Deformed Nuclei

Figure S1: Nuclei deformation is specific to the EMT process: A-B. Quantification of the nuclear aspect ratio (A) and the nuclear deformation index (B) during cellularization and invagination (Cellularization: N=5, n=191; Invagination: N=8, n=431). **C.** Schematic of embryonic transverse section showing regions (ventral, lateral, dorsal) used for analysis in panels D and E. **D-E.** Measurement of nuclear aspect ratio (D) and nuclear deformation index **(E)** during invagination in different regions (Ventral: N=8, n=431; Lateral: N=3, n=176; Dorsal: N=3, n=154). **F.** Transverse sections of wt embryos stained for Lamin Dm0 during the invagination process. Nuclear and cellular morphology is indicated by yellow lines. Dashed lines indicate apical and basal tissue sides. The depth of the nucleus is measured from the apical surface of the embryo. Note the heterogeneity of nuclear depth within the embryo. **G.** Schematic of EMT progression (corresponding to yellow lines panel F), showing the correlation between apical constriction, nuclear repositioning and nuclear deformation during the EMT process. **H.** Quantification of the percentage of deformed nuclei in wt embryos as a function of their depth within the epithelium (N=13, n= 626). Statistical significance was assessed by the Mann−Whitney test (FigS1. A, D), Kolmogorov-Smirnov test (FigS1. B, E), (*****=p<0,05; ******=p<0,01; *******=p<0,001). Scale bar = 5 µm.

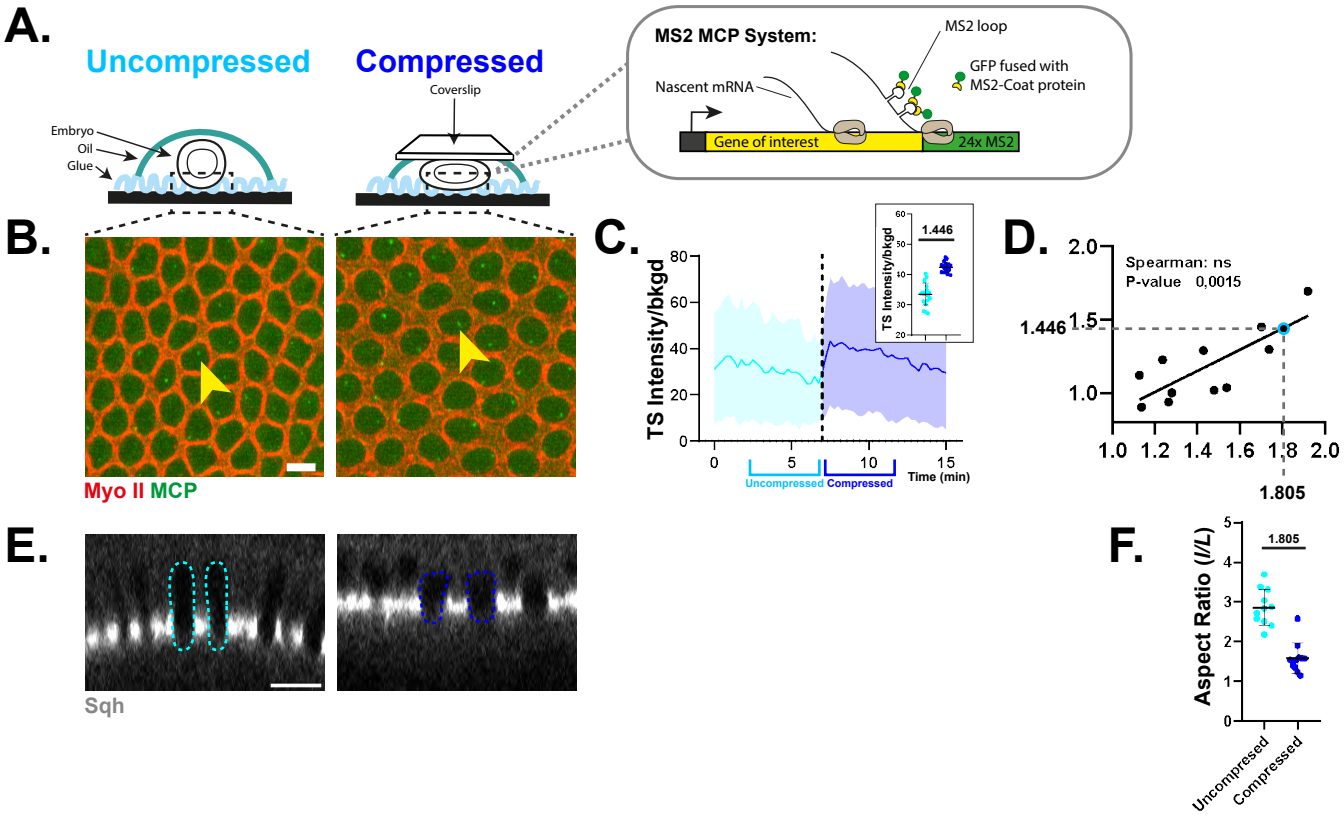
A.
Uncompressed
Compressed
Coverslip
Embryo
Oil
Glue
MS2 MCP System:
MS2 loop
GFP fused with
MS2-Coat protein
Nascent mRNA
Gene of interest
24x MS2
B.
Myo II MCP
C.
TS Intensity/bkgd
Time (min)
Uncompressed
Compressed
1.446
D.
Spearman: ns
P-value 0,0015
1.446
1.805
E.
Sqh
F.
Aspect Ratio (l/L)
1.805
Uncompressed
Compressed

Figure S2: Compression experiments: **A.** Schematic representation of the mechanical compression setup. For detailed description, see Methods. **B.** Time-lapse snapshots of *twist-MS2* Crispr embryos before (left) and after (right) compression. Yellow arrows indicate the same TS over time. MyoII is shown in red, MCP-eGFP (TS) in green. (Related to Fig 2G). **C.** Representative traces of mean normalized TS intensities over time during compression for *twist-MS2* embryos. Light blue indicates before compression, dark blue after compression. The dashed line marks the frame at which compression was applied (t0). The bracket along the x-axis shows the time window used to quantify the TS intensity ratio shown in the inset boxplot (top right), ratio is 1.446. (Related to Fig 2H) **D.** Correlation between variation in TS intensity (ratio before vs after compression) and nuclear deformation in *twist-MS2* Crispr (Related to Fig 2I). **E.** Orthogonal views of embryos before (left) and after (right) compression, MyoII is shown in white. Dashed outlines highlight nuclear edges before (light blue) and after (dark blue) compression. **F.** Quantification of nuclear aspect ratio before and after compression based on nuclei shown in panel E (Before: n=10 nuclei; After: n=10 nuclei). Ratio is 1.805. Note that we use the variation of the nuclear aspect ratio as a readout of nuclear deformation and the level of compression applied during a given compression experiment.

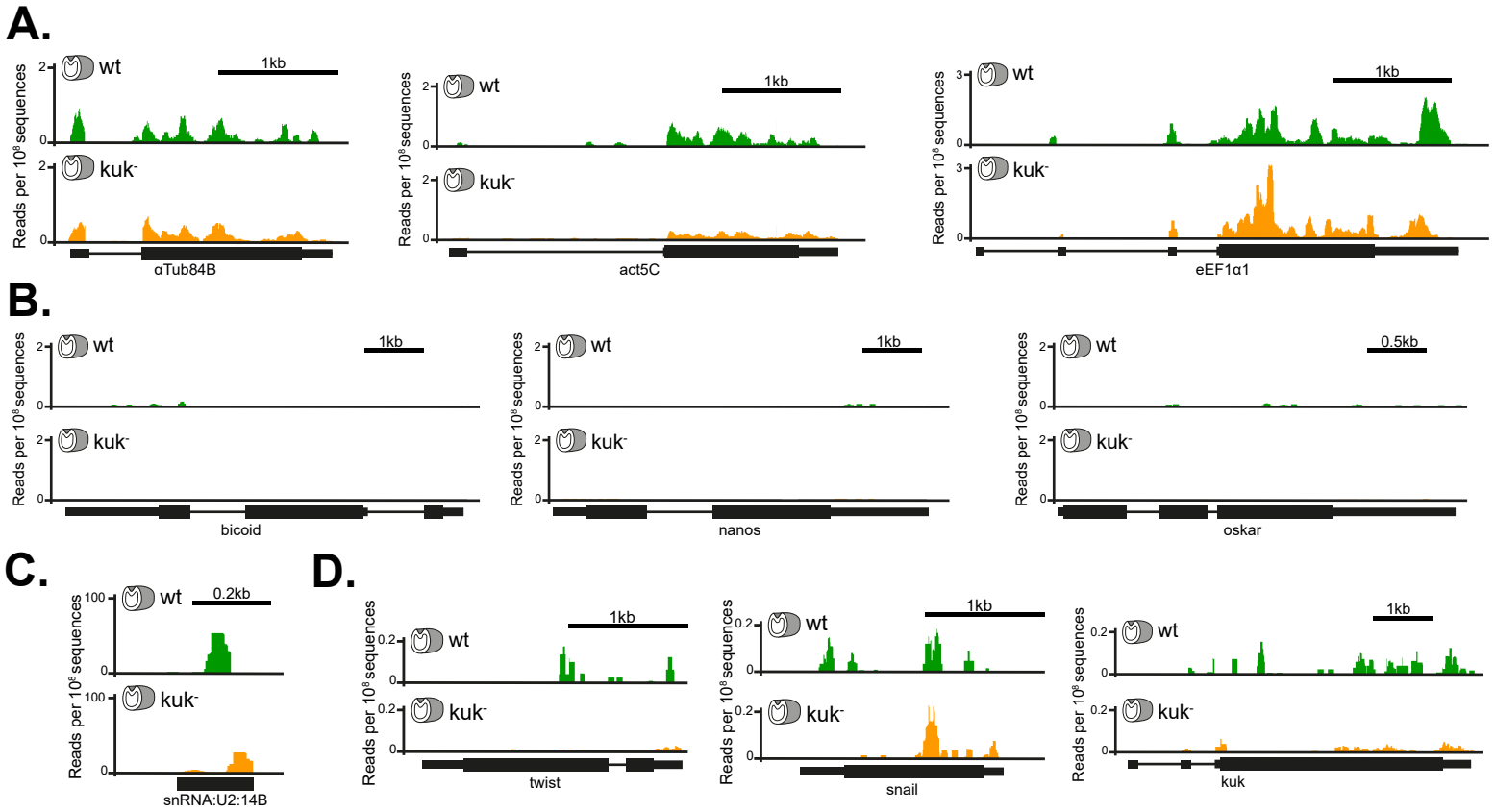
A.
wt
kuk-
1kb
Reads per 10^8 sequences
αTub84B
act5C
eEF1α1
B.
0.5kb
bicoid
nanos
oskar
C.
0.2kb
snRNA:U2:14B
D.
twist
snail
kuk

Figure S3: NET-seq profiles in wild-type and *kuk* mutant embryos during invagination: A. NET-seq profiles for wt and *kuk* mutant embryos during mesoderm invagination for representative housekeeping genes (*αTub84B*, *Act5C*, *eEF1α1*). **B.** NET-seq profiles for maternal genes (*bicoid*, *nanos*, *oskar*) in wt and *kuk* mutant embryos during invagination. **C.** NET-seq profiles for snRNA associated with the RNA Polymerase II complex (*snRNA:U2:14B*) in wt and *kuk* mutant embryos during invagination. **D.** NET-seq profiles for wt and *kuk* mutant embryos during mesoderm invagination for genes of interest (*twist*, *snail*, *kuk*).

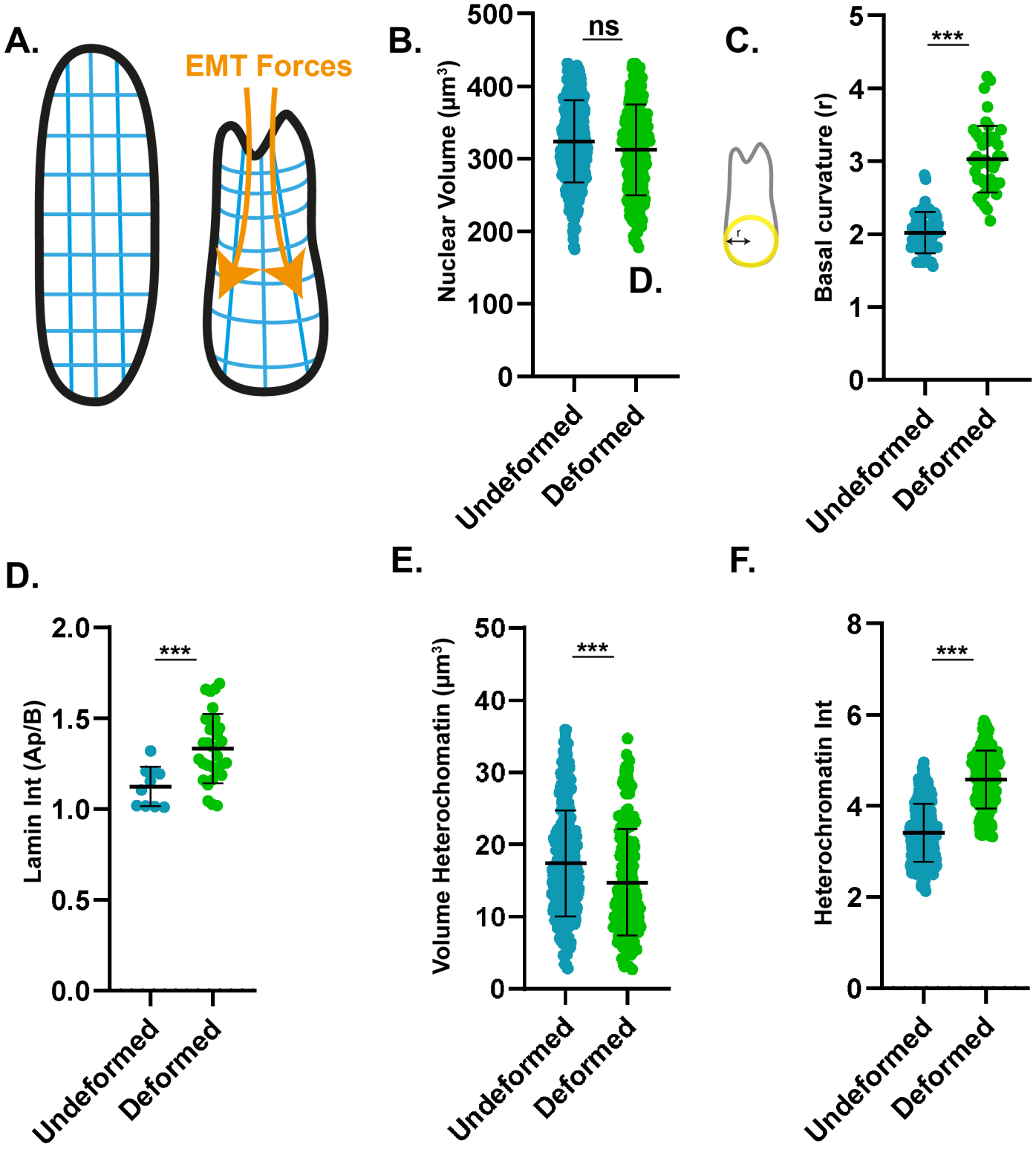
A.
EMT Forces
B.
ns
Nuclear Volume (µm³)
500
400
300
200
100
0
Undeformed
Deformed
C.
***
Basal curvature (r)
5
4
3
2
1
0
Undeformed
Deformed
D.
D.
***
Lamin Int (Ap/B)
2.0
1.5
1.0
0.5
0.0
Undeformed
Deformed
E.
***
Volume Heterochomatin (µm³)
50
40
30
20
10
0
Undeformed
Deformed
F.
***
Heterochromatin Int
8
6
4
2
0
Undeformed
Deformed

Figure S4: EMT forces globally reshape nuclear structure and content: A. Schematic representation showing how EMT-generated forces impact the nucleus globally, deforming both apical and basal regions. **B.** Quantification of nuclear volume in undeformed and deformed nuclei (undeformed: N=13, n=406; deformed: N=13, n=216). **C.** Quantification of basal curvature in undeformed and deformed nuclei (undeformed: N=4, n=60; deformed: N=4, n=45). **D.** Quantification of Lamin Dm0 intensity ratio (apical vs. basal) in undeformed and deformed nuclei (undeformed: N=1, n=10; deformed: N=3, n=29). **E.** Quantification of heterochromatin volume based on DAPI signal in undeformed and deformed nuclei (undeformed: N=3, n=286; deformed: N=3, n=174). **F.** Quantification of total heterochromatin intensity normalized to nuclear mean signal (from DAPI) in undeformed and deformed nuclei (undeformed: N=3, n=286; deformed: N=3, n=174). Statistical significance was assessed by the Mann–Whitney test (*****=p<0,05; ******=p<0,01; *******=p<0,001).

Methods:

Experimental animals

The animal model used here is *Drosophila* melanogaster, in a context of *in vivo/ex vivo* experiments. In order to respect ethic principles, animals were anesthetized with CO2 (adults) before any manipulation. To avoid any release of flies outside the laboratory, dead flies were frozen before throwing them. Stocks of living flies were conserved in incubators, either at 18 or 25 degrees to maintain the flies in optimal condition. Fly food contains water, agar (0.8%), sugar (4%), flour (7.4%), yeast (2.8%), moldex (1%) and propionic acid (0.3%). Genotypes and developmental stages are indicated below. Experiments were performed in both males and females indifferently.

Drosophila Stocks

The w[*] strain was used as the wild-type control. The *kuk* mutant line (BDSC_16856) was obtained from the Bloomington *Drosophila* Stock Center (BDSC). To monitor transcription in living embryos, we used the *w[*], sqh-RFPtKI[3B]; nos>*MCP-EGFP background combined with either *snail-MS2 knock-in* (Pimmett et al. 2024), *twist-MS2 knock-in* (Pimmett et al. 2025), or *snail-MS2* inserted in a basal (Bothma et al., 2015). For live nuclear envelope visualization, we used the Nup107-GFP line from BDSC (BDSC_35514) and a Lamin Dm0 knock-in TagRFPt (Ambrosini et al. 2019) .

All crosses and embryo collections were performed at 25 °C, except for the NET-seq experiments (see **NET-seq** section in *Methods* for details).

Immunohistochemistry

Embryos were collected after a 2-hour egg-laying period, followed by an additional 2-hour incubation, then dechorionated with 50% bleach solution for 2 minutes. Embryos were fixed for 5 min in heptane: formaldehyde 37% (1:1) at 4°C in a rotary agitator. Embryos were washed 2 times with PBS with 0.3% Triton X-100 (PBT). Embryos were selected and sliced with a micro scalpel (Micro Knives-Plastic Handle 10315-12 from Fine Science Tools).

Slices of embryos were blocked with PBT and 0.5% Bovine serum albumin (BBT) followed by overnight incubation at 4°C with appropriate dilutions of primary antibodies in BBT-mouse anti-Lamin (1:10 ADL67.10 from DSHB), rat anti-alpha Tub Tyrosinated (1:50 YL1/2 from Millipore). After BBT washes, slices of embryos were incubated for 4h at room temperature with goat anti-mouse Alexa Fluor 488 (1:100 Interchim) and if necessary, Rhodamine-Phalloidin (1:200 Fischer Scientific). Then, samples were

washed in PBT, and finally mounted between two coverslips with a 120 µm deep spacer (Secure-SealTM, Sigma-Aldrich) in Vectashield containing DAPI (Vectors Laboratories).

smiFISH:

Custom smiFISH probes were designed to target CDS of genes of interest by using the Stellaris® RNA FISH Probe Designer (Biosearch Technologies, Inc., Petaluma, CA) available online at www.biosearchtech.com/stellarisdesigner and coupled with FLAP (X or Y depending the probe) sequence (Tsanov et al. 2016). The smiFISH-FLAP probes were generated by Integrated DNA Technologies (IDT).

Embryos were collected, fixed and sliced as described above for immunohistochemistry. Slices of embryos were washed first with PBS + 1% Tween 20, Followed with 50:50 PBS Tween 20 and Wash Buffer A (20 % Stellaris RNA FISH Wash Buffer A (LGC Biosearch Technologies Cat# SMF-WA1-60, 70% H2O, 10% deionized formamide). Samples are then incubated for 1h at 37°C in the dark in Hybridization Buffer (10 % Deionized Formamide, 90% Stellaris RNA FISH Hybridization Buffer (LGC Biosearch Technologies Cat# SMF-HB1-10). Slices of embryos were incubated overnight in Hybridization Buffer with the annealed smiFISH probes (50nM per Oligos).

SmiFISH probes were prepared by duplexing 40pmol of target-specific probes with 100pmol FLAPX-Cy3 or FLAPY-Cy5 oligonucleotides in annealing Buffer (1X NEBuffer™ 3.1) for 3min at 85°C, 3min at 65°C and 5min at 25°C and kept on ice until use. Following overnight hybridization, embryos were successively washed at 37°C with Hybridization Buffer and Wash Buffer A, followed by a room temperature washed. Immunohistochemistry was then performed if necessary.

Image Acquisition of fixed samples:

Fixed samples were imaged using an LSM900 inverted laser scanning confocal microscope (Ziess), using a 40x/1.3 oil objectives and a piezo stage. Z-stacks were acquired using the laser scanning the High-Resolution mode (Airyscan). Airyscan Z-stacks were processed in ZEN software using the automatic strength (default) and the 3D method.

Compression experiment:

For compression experiments, embryos were collected after a 2-hour egg-laying period, followed by an additional 2-hour incubation. The embryos were then dechorionated by immersion in a 50% bleach solution for 2 minutes.

Following dechorionation, embryos were transferred to an agar plate (20 g/L) and covered with Halocarbon Oil to prevent dehydration and facilitate staging; they could be maintained in these conditions for up to 2 hours.

To ensure stability during compression, cover slips were attached to a metallic support to prevent bending or any form of movement of the cover slips. Glue prepared by incubating Scotch™ double-sided tape in heptane overnight and was applied to the center of the cover slip. One Embryo was gently rolled on the agar surface (avoiding oil) to allow a proper adhesion, and then glued to the prepared cover slip. A drop of 1 µL of Halocarbon Oil was then added to cover the embryo. Samples were imaged using a Zeiss LSM880 confocal microscope in Fast Airyscan mode with Plan-Apochromat 40x/NA 1.3 Oil DIC UV-IR M27 objective at 2x zoom. Time-lapse imaging was performed with a frame interval of 15 seconds. A 488 nm laser at 8% laser power with 850 V gain to detect the MCP-EGFP signal and a 561 laser at 8% laser power with 850 V gain to detect the Sqh-RFPtag signal. Images were captured as 16 bit, with 568×568 pixel resolution, with each pixel being 0.18 µm in length and width with a Z spacing of 0.35 µm. Airyscan Z-stacks were processed in ZEN software using the automatic strength (default) and the 3D method.

During imaging, the orthogonal view in ZEN software was used to observe the cellularization process through the Sqh signal. When cellularization reached the basal side of the nuclei, a 22×22 mm coverslip was gently drop on the sample between two time-frames, resulting in compression of one third of the embryo (data not shown). For each experiment the level of compression were quantify by measuring the nuclear aspect ratio before and after compression.

NET-seq:

Embryo collection and fixation

All the embryo collections were performed at 22°C. Female adult flies were allowed to lay eggs for half an hour on an apple juice-agar plate supplemented with fresh yeast. For the pool of cellularized embryos (nc14 stage), the plate was collected two hours later, as opposed to three hours for the gastrulating one. Harvested embryos were dechorionated then washed in PBT and water. Additional washes were performed in 120 mM NaCl, 0.04% Triton then twice in 120 mM NaCl before freezing the embryos in liquid nitrogen. After fixation, embryos were stored at -80°C.

Net-seq and library preparation

The protocol was adapted from the dNET-seq protocol developed previously (Prudêncio et al. 2022). Slight modifications are listed below.

In order to optimize chromatin precipitation and avoid material loss during nuclear extraction, 600 uL of frozen embryos were resuspended, homogenized in a Dounce homogenizer. Their nuclei were extracted and the samples were divided in three independents pools before the chromatin precipitation.

Immunoprecipitation of Pol II-RNA complexes was performed using sheep anti-mouse Dynabeads (ThermoFisher), preincubated overnight with the anti-Pol II CTD S2P antibody (gift from Dr H. Kimura).

The RNAs were selected based on their size on a precast 6% TBE urea gel (Thermofisher) using SYBR™ Gold (Thermofisher) for nucleotide staining. RNA comprised between 30 and 150nt were excised from the gel to proceed to library preparation after gel extraction. An amount of 100 ng of RNA was used to prepare each library, following the standard protocol of the NEBNext® Small RNA Library Prep Set for Illumina®. After adapter ligation and reverse transcription, the libraries were PCR amplified using 15 PCR cycles. cDNA libraries were fractionated using CleanNGS magnetic Beads to remove fragments smaller than 130bp that include primers and dimers of primers from the libraries. The libraries were sequenced using Novaseq SP 1 FC SR100/PE50 (Mgx plateform, Montpellier).

Differential analysis

Read pairs were trimmed using Cutadapt (version 1.13 with Python 3.4.5) (Martin 2011) to remove adapter sequences (-m 10 -e 0.05 --match-read-wildcards -n 1). For DESeq analysis, the remaining paired-end reads were aligned to the *Drosophila* reference genome (dm6) using STAR (version 2.7). Only uniquely mapped reads were retained, extracted with SAMtools(version 0.1.19) (Li et al. 2009). Gene raw counts were obtained using HTSeq-count (version 0.6.1p1) (Anders et a., 2015), and these counts were subsequently used as input for DESeq (Anders et al. 2015) analysis.

Exceptionally, for the generation of signal bigwig files, reads matching ribosomal RNA sequences and the yeast genome were filtered out. The remaining reads were then aligned to the reference genome using STAR (v2.6.0b) (Dobin et al. 2013). As before, only uniquely mapped reads were kept, extracted with SAMtools (version 0.1.19) (Li et al. 2009), and converted to coverage signal files using bamCoverage from deepTools (version 3.3.0) (Ramírez et al. 2016).

Gene positioning

The relative gene position within the nucleus was evaluated based on their distance to the centromere, following the proposed nuclear organization of chromosomes in early *Drosophila* embryos. This organization was supported by the correlation between mean nuclear positions obtained by smiFISH (*zfh1*, *twi*, *T48*, *sna*_bac (*CG8552*), *brd*, *sim*, *sna*, *Ncad*) and the calculated distances to centromeres.

This correlation was previously tested for chromosomes 2 **(Marshall et al. 1996).** . We took genes from chromosome II (n=5) and III (n=4) and found a correlation of slope = 0.6907, Y-intercept = 0.1585.

The distance to the centromere was calculated differently depending on the chromosomal arm orientation. For left arms (2L and 3L), where the centromere is located at the end of the sequence, the formula used was: (1 – (gene position / chromosome size)) * 0.6907 + 0.1585

For right arms (2R and 3R), where the centromere is located at the beginning of the sequence, the formula was: (gene position / chromosome size) * 0.6907 + 0.1585

Gene position was calculated as the mean coordinate between the start and end of the coding sequence (CDS). The chromosome sizes used in the calculations were: 2L: 23,493,794 bp; 2R: 25,286,936 bp; 3L: 28,090,333 bp; 3R: 32,079,331 bp (data from Flybase).

For the different gene subsets, these calculations were performed automatically using a custom Python script.

Optical Tweezer:

Set up

A home-built setup was used for optical trapping measurements. The system combines a fluorescence microscope and an active optical trapping system. This trapping system has two components: one to precisely control the position of the optical trap on the sample, and a back focal plane interferometric (BFPi) system to track the position of the trapped object relative to the center of the laser (Allersma et al. 1998; Gittes and Schmidt 1998). Furthermore, the use of back focal interferometry in tissue is also unaffected by the light's scattering due to its position in the Fourier plane of the detector (Merle et al. 2025).

For calibration and the measurements described below, a steering mirror conjugated to the pupil plane of the microscope (Thorlabs FSM75-P01) is used to achieve nanometric laser deflection. A 3-axis piezoelectric stage (Piezo Concept BIO3) is also used to precisely focus on the trapped object.

The optical trapping system is implemented in a conventional inverted fluorescence microscope (Leica DMI6000 B). The objective lens used is a 100x magnification lens with a numerical aperture of 1.4 (Leica HCX PL APO). To optimize the fill factor of the infrared laser to 85% of the objective lens pupil plane, an X4 afocal telescope consisting of two relay lenses is used (Thorlabs ACA254-050-1064 and ACA254-200-1064). The focused diffraction spot at the objective exit has a width of 600 nm at mid-height, allowing for an efficient optical trap.

The microscope is optimized for simultaneous GFP and RFP imaging combined with the infrared laser trap, thanks to a 3-band dichroic mirror (Semrock Di03-R405/488/561/635-t1-25x36). Imaging and optical tweezers are controlled by combining a National Instruments acquisition card with the Inscoper synchronization box. The Inscoper software manages all synchronization steps.

Optical Tweezers calibration and rigidity measurements

An internal lipid droplet (refractive index ~1.5, average diameter ~300 nm) was first captured and used as a probe. The laser used for trapping was centered at 1064 nm, and the power delivered to the sample was 3.8 A for the WT and 5 A for the *Kuk* mutant. At this wavelength and power, tissue behavior is not affected.

Immediately after trapping, the optical tweezers were calibrated for each measurement using the fluctuation-dissipation theorem (FDT) at a high frequency of 1 kHz, which enables the simultaneous estimation of trap stiffness (k), the detector, and the FDT method. A 360 nm, 2.3 Hz square laser displacement was then applied and tracked using back focal plane interferometry to calibrate the system and determine the membrane's elasticity.

This confirmed the data obtained using the FDT method. A lipid droplet was then trapped and used to indent the nucleus at a depth of 1.5 µm using a fast piezoelectric stage. The droplet was then held at an equilibrium position (Venturi et al., 2020). After calibrating the optical tweezers using the FDT method, the relaxation force is plotted. After three seconds, the force profile reaches equilibrium between the force induced by the nucleus and the optical tweezers. This value can be used to calculate the tension of the nucleus, the conversion factor (β, V/nm) and the elastic response of the medium or nucleus membrane, even in a heterogeneous environment (Fischer et al., 2010; Hendricks et al., 2012). This method combines passive and active rheology using fast, small, laser-driven stimulation. In this paper, the method draws inspiration from a multiplexed FDT method (Yan et al., 2017) to enhance the efficiency of the process using an active, square, laser-driven sequence. The optical trap is calibrated for each measurement using a 7-second recording of passive and active trajectories consisting of a 2.3 Hz square pattern at the highest frequency.

To test this method, a droplet was pushed against the nuclear envelope at a depth of 1.5 µm, and the FDT method with a 360 nm, 2.3 Hz square laser displacement was applied and tracked using back focal plane interferometry to calibrate the system and determine the elasticity.

Then, the trap was deactivated, and the droplet moved away from the nucleus, allowing observation of nuclear relaxation in fluorescence.

Force Induction & Transcription response

For this experiment, the same home-built setup used for optical trapping measurements was employed. To deform nuclei and monitor the transcriptional response, an automated acquisition sequence was designed as follows:

Phase 1: Pre-indentation: The 488 nm led was focused at 15% power; the optical trap was inactive. Z-stack acquisition of 15 slices with a 0.4 µm step size was performed, repeated 20 times at 1.5 seconds per stack.

Phase 2: Indentation: The 488 nm led remained focused at 15% power; the optical trap was activated using a 500 nm square wave modulation at 0.5 Hz. Z-stack acquisition of 15 slices with a 0.4 µm step size was again repeated 20 times at 1.5 seconds per stack.

Phase 3: Brightfield snapshot: A single-plane brightfield image was captured at the center of the Z-stack, corresponding to the trap's focal plane.

Prior to launching the automated sequence, nuclei were selected based on the presence of an active transcription site (TS). The trap, initially inactive, was positioned as close as possible to the nuclear envelope, identified in brightfield imaging by the contrast difference between the nucleus and cytoplasm. This positioning method was the same as described in Figure 4A for nuclear deformation.

The trap position was determined using a predefined region of interest (ROI) set before the start of the experiment. To enhance the signal-to-noise ratio, 2×2 pixel binning was applied. Successful indentation was validated by visually confirming nuclear deformation in the brightfield snapshot acquired at the trap focal plane.

Quantification and statistical analysis:

Nuclear segmentation

Nuclei segmentation was performed using immunofluorescence staining with an anti-Lamin Dm0 antibody. Cellpose (Stringer et al. 2021), configured with the cyto2 model, was used for segmentation, applying a flow threshold of 0.4 and adjusting the estimated cell diameter per image to optimize results. The resulting labels were then filtered with the MorphoLibJ plugin (Legland et al. 2016) using Label Size Filtering (Greater_Than; Size Limit: 50,000 pixels). The central (middle) plane of each nuclear mask was extracted using a custom macro in Fiji. Given the variability in nuclear orientation, each nucleus was re-aligned with the image's y-axis to minimize artifacts in aspect ratio and deformation index measurements. Quantification was restricted to nuclei located within the invagination.

Nuclear aspect ratio and Volume

Nuclear aspect ratio and volume were quantified using Label Analyzer (2D,3D) from the SCF-MPICBG plugin in Fiji (Version 1.2.0).

Deformation index

The deformation index was analyzed only in the apical and not over the whole nucleus. The upper part of each nucleus was defined using coordinates obtained from the "Label Analyzer (2D, 3D)" of the SCF-MPICBG plugin, based on the center of mass and bounding box. Based on a selection of the upper part of the nucleus, angles were calculated using the Array.getVertexAngle function from Fiji. The deformation index for each nucleus was defined as the mean of the top 10% maximum angles. These angles were also used to compare their distribution between in wild-type and *kuk* mutant nuclei.

% Deformed Nucleus

Based on the angles calculated for the deformation index, a nucleus was classified as deformed if it contained at least one angle greater than 60°. This threshold was chosen because it showed the most significant contrast between embryos at the cellularization stage, which predominantly contain undeformed nuclei, and embryos during invagination, which mainly exhibit deformed nuclei (data not shown).

Nuclei 3D reconstruction

Based on the segmented nuclear masks, 3D reconstructions were generated using the Surface tool in IMARIS.

smiFISH TS analysis

smiFISH analysis was performed using previously published custom Python software (Dufourt et al. 2021) available online: https://github.com/ant-trullo/smFiSH_software. From this analysis, we extracted all TS, with their normalized intensities and 3D positions. Using the same method as for quantifying the "% of deformed nuclei" but applied manually. We determined, in the smiFISH images, which nuclei were deformed or not. For each nucleus, we then assessed whether it contained TS. If the TS coordinates identified manually in Fiji were also confirmed by the Python analysis, the TS was validated and counted. This approach allowed us to quantify the "number of active TS" and the "TS intensity per nucleus" which corresponds to the sum of normalizes intensities of all TS within a given nucleus. TS positions along the apico-basal axis were analyses manually on Fiji.

Compression experiment

Live transcription was analyze using a features (detection and tracking MS2/MCP TS in the absence of a nuclear marker) of a custom Python software previously published (Pimmett et al. 2025) available online: https://github.com/ant-trullo/OptoTrack. From this analysis, we extracted all TS with their normalized intensities and 3D positions. Only tracks with a duration of at least 10% of the total imaging time were retained for analysis. The "Intensity Ratio" before and after compression was calculated as the ratio of the mean intensity of all tracks during the 5 minutes (corresponding to 20-time frames) before and after compression.

The “Nucleus deformation” were manually assessed in Fiji, based on the shadow projected by the nucleus in the Sqh signal. 10 nuclei were quantified after and before to do the “Nucleus deformation” ratio also use as a read out of the level compression apply for each experiment.

Transcription response to Force induction:

Movies recorded with the trap off and on were concatenated. Only movies in which TS remained entirely within the Z-stack throughout the acquisition were included in the analysis. Prior to analysis, bleach correction and bandpass filtering were applied in Fiji. The same Python-based software used for the compression experiments was then employed for quantification.

The distance between the TS and the trap was calculated using the 3D coordinates of the TS extracted from the first frame and the trap position, defined by a manually placed ROI during the experiment and register within the movie metadata.

The "TS Intensity Ratio" was defined as the ratio between the mean normalized intensity of the last 10 frames with the trap off and the mean normalized intensity of the last 10 frames with the trap on. For each experiment, one TS from an unmanipulated nucleus was used as a control.

Optical Tweezers: Relaxion

Nuclear relaxation was assessed by comparing the nuclear area in 2D before and after the indentation phase. A nucleus was considered to have undergone complete relaxation if its area after indentation (end of the movie) comprised at least 95% of its area before indentation (beginning of the movie). Values below this threshold were classified as partial relaxation. Note: none of the indentations were maintained. Nuclear areas were manually measured using Fiji.

Heterochromatin analysis:

Heterochromatin 3D was performed using the DAPI staining. Cellpose configured with the cyto2 model, was used for segmentation, applying a flow threshold of 0.4 and adjusting the estimated cell diameter per image to optimize results. Volume and total intensity were quantified using Label Analyzer (2D,3D)

from the SCF-MPICBG plugin in Fiji (Version 1.2.0). Total intensity values were normalized to the mean DAPI signal of the euchromatin.

Lamin analysis:

A Lamin-RFP knock-in line was used to visualize the lamin signal along the nuclear envelope at the nuclear mid-plane. A custom Fiji macro was developed to extract the signal around the entire nuclear contour. Apical and basal regions were defined as the top 25% and bottom 25% of positions, respectively, relative to the mean vertical position of each nucleus. The apical-to-basal intensity ratio was then calculated and plotted.

References

Allersma, M. W., F. Gittes, M. J. deCastro, R. J. Stewart, and C. F. Schmidt. 1998. "Two-Dimensional Tracking of Ncd Motility by Back Focal Plane Interferometry." *Biophysical Journal* 74 (2 Pt 1): 1074–85. https://doi.org/10.1016/S0006-3495(98)74031-7.

Ambrosini, Arnaud, Mégane Rayer, Bruno Monier, and Magali Suzanne. 2019. "Mechanical Function of the Nucleus in Force Generation during Epithelial Morphogenesis." *Developmental Cell* 50 (2): 197-211.e5. https://doi.org/10.1016/j.devcel.2019.05.027.

Anders, Simon, Paul Theodor Pyl, and Wolfgang Huber. 2015. "HTSeq--a Python Framework to Work with High-Throughput Sequencing Data." *Bioinformatics (Oxford, England)* 31 (2): 166–69. https://doi.org/10.1093/bioinformatics/btu638.

Bothma, Jacques P., Hernan G. Garcia, Samuel Ng, Michael W. Perry, Thomas Gregor, and Michael Levine. 2015a. "Enhancer Additivity and Non-Additivity Are Determined by Enhancer Strength in the Drosophila Embryo." *eLife* 4 (August): e07956. https://doi.org/10.7554/eLife.07956.

Bothma, Jacques P., Hernan G. Garcia, Samuel Ng, Michael W. Perry, Thomas Gregor, and Michael Levine. 2015b. "Enhancer Additivity and Non-Additivity Are Determined by Enhancer Strength in the Drosophila Embryo." *eLife* 4 (August): e07956. https://doi.org/10.7554/eLife.07956.

Calderon, Diego, Ronnie Blecher-Gonen, Xingfan Huang, et al. 2022. "The Continuum of Drosophila Embryonic Development at Single-Cell Resolution." *Science* 377 (6606): eabn5800. https://doi.org/10.1126/science.abn5800.

Cho, Sangkyun, Jerome Irianto, and Dennis E. Discher. 2017. "Mechanosensing by the Nucleus: From Pathways to Scaling Relationships." *The Journal of Cell Biology* 216 (2): 305–15. https://doi.org/10.1083/jcb.201610042.

Comings, D. E. 1980. "Arrangement of Chromatin in the Nucleus." *Human Genetics* 53 (2): 131–43. https://doi.org/10.1007/BF00273484.

Desprat, N., W. Supatto, P. A. Pouille, E. Beaurepaire, and E. Farge. 2008. "Tissue Deformation Modulates Twist Expression to Determine Anterior Midgut Differentiation in Drosophila Embryos." In *Dev Cell*, No. 3, vol. 15. no. 3. https://doi.org/10.1016/j.devcel.2008.07.009.

Dobin, Alexander, Carrie A. Davis, Felix Schlesinger, et al. 2013. "STAR: Ultrafast Universal RNA-Seq Aligner." *Bioinformatics (Oxford, England)* 29 (1): 15–21. https://doi.org/10.1093/bioinformatics/bts635.

Dufourt, Jeremy, Maelle Bellec, Antonio Trullo, et al. 2021. "Imaging Translation Dynamics in Live Embryos Reveals Spatial Heterogeneities." *Science (New York, N.Y.)* 372 (6544): 840–44. https://doi.org/10.1126/science.abc3483.

Dupont, Sirio, and Sara A. Wickström. 2022. "Mechanical Regulation of Chromatin and Transcription." *Nature Reviews. Genetics* 23 (10): 624–43. https://doi.org/10.1038/s41576-022-00493-6.

Elosegui-Artola, A., I. Andreu, A. E. M. Beedle, et al. 2017. "Force Triggers YAP Nuclear Entry by Regulating Transport across Nuclear Pores." In *Cell*, No. 6, vol. 171. no. 6. https://doi.org/10.1016/j.cell.2017.10.008.

Farge, E. 2003. "Mechanical Induction of Twist in the Drosophila Foregut/Stomodeal Primordium." In *Curr Biol*, No. 16, vol. 13. no. 16. https://doi.org/10.1016/s0960-9822(03)00576-1.

Font-Noguera, Meritxell, Marianne Montemurro, Corinne Benassayag, Bruno Monier, and Magali Suzanne. 2021. "Getting Started for Migration: A Focus on EMT Cellular Dynamics and Mechanics in Developmental Models." *Cells & Development* 168 (December): 203717. https://doi.org/10.1016/j.cdev.2021.203717.

Gelbart, M. A., B. He, A. C. Martin, S. Y. Thiberge, E. F. Wieschaus, and M. Kaschube. 2012. "Volume Conservation Principle Involved in Cell Lengthening and Nucleus Movement during Tissue Morphogenesis." In *Proc Natl Acad Sci U S A*, No. 47, vol. 109. no. 47. https://doi.org/10.1073/pnas.1205258109.

Gittes, F., and C. F. Schmidt. 1998. “Interference Model for Back-Focal-Plane Displacement Detection in Optical Tweezers.” *Optics Letters* 23 (1): 7–9. https://doi.org/10.1364/ol.23.000007.

Hsia, Chieh-Ren, Jawuanna McAllister, Ovais Hasan, et al. 2022. “Confined Migration Induces Heterochromatin Formation and Alters Chromatin Accessibility.” *iScience* 25 (9): 104978. https://doi.org/10.1016/j.isci.2022.104978.

Ing-Simmons, Elizabeth, Roshan Vaid, Xin Yang Bing, Michael Levine, Mattias Mannervik, and Juan M. Vaquerizas. 2021. “Independence of Chromatin Conformation and Gene Regulation during Drosophila Dorsoventral Patterning.” *Nature Genetics* 53 (4): 487–99. https://doi.org/10.1038/s41588-021-00799-x.

Killaars, Anouk R., Joseph C. Grim, Cierra J. Walker, Ella A. Hushka, Tobin E. Brown, and Kristi S. Anseth. 2019. “Extended Exposure to Stiff Microenvironments Leads to Persistent Chromatin Remodeling in Human Mesenchymal Stem Cells.” *Advanced Science (Weinheim, Baden-Wurttemberg, Germany)* 6 (3): 1801483. https://doi.org/10.1002/advs.201801483.

Legland, David, Ignacio Arganda-Carreras, and Philippe Andrey. 2016. “MorphoLibJ: Integrated Library and Plugins for Mathematical Morphology with ImageJ.” *Bioinformatics* 32 (22): 3532–34. https://doi.org/10.1093/bioinformatics/btw413.

Li, Heng, Bob Handsaker, Alec Wysoker, et al. 2009. “The Sequence Alignment/Map Format and SAMtools.” *Bioinformatics* 25 (16): 2078–79. https://doi.org/10.1093/bioinformatics/btp352.

Marshall, W. F., A. F. Dernburg, B. Harmon, D. A. Agard, and J. W. Sedat. 1996. “Specific Interactions of Chromatin with the Nuclear Envelope: Positional Determination within the Nucleus in Drosophila Melanogaster.” *Molecular Biology of the Cell* 7 (5): 825–42. https://doi.org/10.1091/mbc.7.5.825.

Martin, Marcel. 2011. “Cutadapt Removes Adapter Sequences from High-Throughput Sequencing Reads.” *EMBnet.Journal* 17 (1): 1. https://doi.org/10.14806/ej.17.1.200.

Maurer, M., and J. Lammerding. 2019. “The Driving Force: Nuclear Mechanotransduction in Cellular Function, Fate, and Disease.” In *Annu Rev Biomed Eng*, vol. 21. https://doi.org/10.1146/annurev-bioeng-060418-052139.

Merle, Tatiana, Martine Cazales, Ronan Bouzignac, Brice Ronsin, Christian Rouvière, and Magali Suzanne. 2025. “Compressive Stress Drives Morphogenetic Apoptosis.” *Cell Reports*, August, 2024.02.08.579454. https://doi.org/10.1101/2024.02.08.579454.

Na, Sungsoo, Olivier Collin, Farhan Chowdhury, et al. 2008. “Rapid Signal Transduction in Living Cells Is a Unique Feature of Mechanotransduction.” *Proceedings of the National Academy of Sciences of the United States of America* 105 (18): 6626–31. https://doi.org/10.1073/pnas.0711704105.

Nava, M., Y. A. Miroshnikova, L. C. Biggs, et al. 2020. “Heterochromatin-Driven Nuclear Softening Protects the Genome against Mechanical Stress-Induced Damage.” In *Cell*, No. 4, vol. 181. no. 4. https://doi.org/10.1016/j.cell.2020.03.052.

Pimmett, Virginia, Douaihy, Maillard, et al. 2024. “Coordinated Active Repression Operates via Transcription Factor Cooperativity and Multiple Inactive Promoter States in a Developing Organism.” *bioRxiv*. doi: https://doi.org/10.1101/2024.11.28.623729, in Press Nature Comms.

Pimmett, Virginia L., James McGehee, Antonio Trullo, et al. 2025. “Optogenetic Manipulation of Nuclear Dorsal Reveals Temporal Requirements and Consequences for Transcription.” *Development (Cambridge, England)* 152 (6): dev204706. https://doi.org/10.1242/dev.204706.

Prudêncio, Pedro, Rosina Savisaar, Kenny Rebelo, Rui Gonçalo Martinho, and Maria Carmo-Fonseca. 2022. “Transcription and Splicing Dynamics during Early Drosophila Development.” *RNA (New York, N.Y.)* 28 (2): 139–61. https://doi.org/10.1261/rna.078933.121.

Ramírez, Fidel, Devon P. Ryan, Björn Grüning, et al. 2016. “deepTools2: A next Generation Web Server for Deep-Sequencing Data Analysis.” *Nucleic Acids Research* 44 (W1): W160-165. https://doi.org/10.1093/nar/gkw257.

Solovei, Irina, Moritz Kreysing, Christian Lanctôt, et al. 2009. “Nuclear Architecture of Rod Photoreceptor Cells Adapts to Vision in Mammalian Evolution.” *Cell* 137 (2): 356–68. https://doi.org/10.1016/j.cell.2009.01.052.

Stephens, A. D., E. J. Banigan, S. A. Adam, R. D. Goldman, and J. F. Marko. 2017. “Chromatin and Lamin A Determine Two Different Mechanical Response Regimes of the Cell Nucleus.” In *Mol Biol Cell*, No. 14, vol. 28. no. 14. https://doi.org/10.1091/mbc.E16-09-0653.

Stringer, Carsen, Tim Wang, Michalis Michaelos, and Marius Pachitariu. 2021. “Cellpose: A Generalist Algorithm for Cellular Segmentation.” *Nature Methods* 18 (1): 100–106. https://doi.org/10.1038/s41592-020-01018-x.

Sun, Jian, Junwei Chen, Kshitij Amar, Yanyan Wu, Mingxing Jiang, and Ning Wang. 2023. “LAP2β Transmits Force to Upregulate Genes via Chromatin Domain Stretching but Not Compression.” *Acta Biomaterialia* 163 (June): 326–38. https://doi.org/10.1016/j.actbio.2021.10.029.

Sun, Jian, Junwei Chen, Erfan Mohagheghian, and Ning Wang. 2020. “Force-Induced Gene up-Regulation Does Not Follow the Weak Power Law but Depends on H3K9 Demethylation.” *Science Advances* 6 (14): eaay9095. https://doi.org/10.1126/sciadv.aay9095.

Sun, Jingjing, Chen Zhang, Fan Gao, and Angelike Stathopoulos. 2023. “Single-Cell Transcriptomics Illuminates Regulatory Steps Driving Anterior-Posterior Patterning of Drosophila Embryonic Mesoderm.” *Cell Reports* 42 (10). https://doi.org/10.1016/j.celrep.2023.113289.

Tajik, A., Y. Zhang, F. Wei, et al. 2016. “Transcription Upregulation via Force-Induced Direct Stretching of Chromatin.” In *Nat Mater*, No. 12, vol. 15. no. 12. https://doi.org/10.1038/nmat4729.

Tsanov, Nikolay, Aubin Samacoits, Racha Chouaib, et al. 2016. “smiFISH and FISH-Quant - a Flexible Single RNA Detection Approach with Super-Resolution Capability.” *Nucleic Acids Research* 44 (22): e165. https://doi.org/10.1093/nar/gkw784.

Wang, Ning, Jessica D. Tytell, and Donald E. Ingber. 2009. “Mechanotransduction at a Distance: Mechanically Coupling the Extracellular Matrix with the Nucleus.” *Nature Reviews. Molecular Cell Biology* 10 (1): 75–82. https://doi.org/10.1038/nrm2594.

Yang, J., P. Antin, G. Berx, et al. 2020. “Guidelines and Definitions for Research on Epithelial-Mesenchymal Transition.” In *Nat Rev Mol Cell Biol*, No. 6, vol. 21. no. 6. https://doi.org/10.1038/s41580-020-0237-9.